

1

2 The Physics Behind the CosmicWatch Desktop Muon 3 Detectors

4

5

December 20, 2018

6
7 The CosmicWatch Desktop Muon Detector is a Massachusetts Institute of Technology (MIT) and Polish National Center for Nuclear Research (NCBJ) based undergraduate-level
8 physics project that incorporates various aspects of electronics-shop technical development. The
9 detector was designed to be low-power and extremely portable, which opens up a wide range of
10 physics for students to explore. This document describes the physics behind the Desktop Muon
11 Detectors and explores possible measurements that can be made with the detectors. In particu-
12 lar, we explore various physical phenomena associated with the geomagnetic field, atmospheric
13 conditions, cosmic ray shower composition, attenuation of particles in matter, radioactivity, and
14 statistical properties of Poissonian process.



¹⁷ Contents

¹⁸	1 Document overview	4
¹⁹	2 Sources of ionizing radiation	5
²⁰	2.1 Cosmic radiation	5
²¹	2.1.1 Flux variations due to solar system properties	9
²²	2.1.2 Flux variations due to atmospheric properties	10
²³	2.2 Radioactive backgrounds	11
²⁴	3 Particle interactions with matter	12
²⁵	3.1 High energy heavy charged particles	12
²⁶	3.2 High energy electrons/positrons and photons	14
²⁷	3.3 Low energy electrons/positrons	16
²⁸	3.4 Low energy gamma rays	16
²⁹	3.5 Neutrons	17
³⁰	4 Detection methods	18
³¹	4.1 Single photon detections: photomultipliers	18
³²	4.2 Scintillators	19
³³	5 The CosmicWatch program	21
³⁴	5.1 The Desktop Muon Detector	22
³⁵	5.2 Building and operating the detector	24
³⁶	5.3 Recording data	25
³⁷	5.3.1 Setting detectors in master and coincidence mode	27

³⁸	6 Example measurements	29
³⁹	6.1 A coincidence measurement	31
⁴⁰	6.2 Measuring the cosmic ray muon rate in an airplane at 33,000 ft	32
⁴¹	6.3 High altitude balloon measurement at 107,000 ft	33
⁴²	6.4 Muon rate measurement while flying to the South Pole	35
⁴³	6.5 Latitude correction to the cosmic ray muons	37
⁴⁴	6.6 Cosmic-ray muon rate at various locations on Earth	38
⁴⁵	6.7 Rate measurement 1 km underground at Super-Kamiokande	39
⁴⁶	6.8 Cosmic ray muon angular distribution	41
⁴⁷	6.9 Electromagnetic component of cosmic ray showers	42
⁴⁸	6.10 Correlation between the cosmic ray muon rate and atmospheric pressure	43
⁴⁹	6.11 Reducing the radioactive backgrounds	44
⁵⁰	6.12 Common sources of radioactivity	45
⁵¹	6.13 Portable trigger system for an accelerator beamline	46
⁵²	6.14 A true random number generator	47
⁵³	6.15 The Poissonian nature of radioactive decay	49
⁵⁴	6.16 Future measurements	50
⁵⁵	7 Conclusion	51
⁵⁶	8 Acknowledgements	51
⁵⁷	9 FAQ	51

58 **1 Document overview**

59 This document is concerned with describing the physics associated with the CosmicWatch Desk-
60 top Muon Detectors. It will begin by outlining the forms of ionizing radiation that are capable
61 of triggering the detector. Then, we describe what effect these forms of ionizing radiation have
62 on the detector and why they are important for our consideration. Reading these sections will
63 be useful for those interested in developing their physics knowledge or teaching particle/astro
64 physics in the classroom. We then move to the information specific to the Desktop Muon
65 Detectors, by giving an overview of the technology used and the physics behind them.

66 The latter half of the document is dedicated to illustrating various physical phenomena described
67 in the earlier sections using the detectors. Along the way, we'll briefly mention some fascinating,
68 and perhaps enlightening aspects of physics, which hopefully encourages novices to dive a bit
69 deeper than what we go into here. As new ideas come in, and new data is analyzed, we hope
70 this section will be continuously updated.

71 All supplementary material can be found in the GitHub repository located here:

72 <https://github.com/spenceraxani/CosmicWatch-Desktop-Muon-Detector-v2>

73 There are several documents that have been particularly useful when putting this together. Ex-
74 perience physicists will undoubtedly be familiar with the Particle Data Group's (PDG) summary
75 of cosmic rays [1] and energy loss in matter [2], as it is a fantastic reference. A non-physicist may
76 find Prof. Bruno Rossi's *Cosmic Rays*[3], a great entry level book that gives an early account
77 of the initial investigation into cosmic ray physics. It's a great read, although it obviously does
78 not contain information on our modern understanding, as it was published in 1964. A more
79 modern perspective that particularly focuses on the history can be found in Prof. Michael
80 W. Friedlander's book entitled *A Thin Cosmic Rain*[4]. The most thorough and comprehensive
81 overview of cosmic ray physics can be found in Dr. Peter K. F. Grieder's textbook *Cosmic Rays*
82 at *Earth*[5]; we will be referencing it often. When discussing higher energy cosmic ray physics,
83 Prof. Thomas K. Gaisser's book entitled *Cosmic Rays and Particle Physics*[6] is extremely
84 useful. Although more heavily focused on the neutrino side of cosmic rays and particle physics,
85 Prof. Masataka Fukagita's two textbooks *Physics of Neutrinos* and *Physics of Neutrinos and*
86 *Applications to Astrophysics*[7], was found to often have interesting bits of information that
87 we could not find in the other readings. The overall best description that on energy loss in
88 matter comes from *Techniques for Nuclear and Particle Physics*[8] by William R. Leo, which is
89 a great resource for experimental particle physics. We would also recommend Prof. Claus Grupen's
90 textbook entitled *Particle Detectors*[9], which is a great reference for describing detection
91 methods in particle physics.

92 The CosmicWatch project owes a lot to Dr. Katarzyna Frankiewicz. For both of us, this began
93 as hobby and desire to contribute to the community, and eventually ballooned into a popular
94 and well-developed program thanks in large part to her work. Prof. Janet M. Conrad's support
95 and encouragement throughout the development of this project was equally important to where

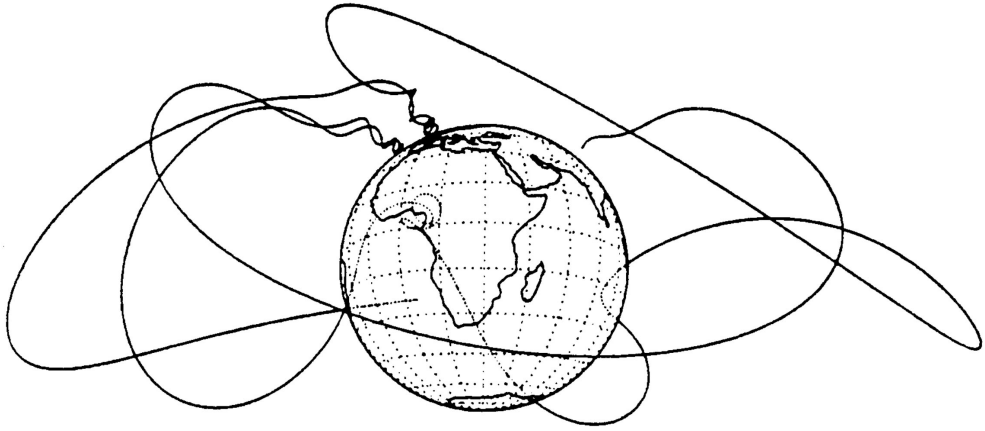


Figure 1: Simulated trajectories of low energy cosmic rays interacting with the geomagnetic field. From Ref. [4]

⁹⁶ the project is now.

⁹⁷ 2 Sources of ionizing radiation

⁹⁸ We'll begin by discussing the various sources of ionizing radiation that are capable of triggering
⁹⁹ the Desktop Muon Detectors. There are a few forms of ionizing radiation that are particularly
¹⁰⁰ important due to their abundances and their energies. In passing, we will also discuss why we
¹⁰¹ are not sensitive to certain other forms of ionizing radiation, however a description of them is
¹⁰² often important for completeness.

¹⁰³ 2.1 Cosmic radiation

¹⁰⁴ The Earth is continuously being bombarded by a flux of particles called *cosmic rays*. Ap-
¹⁰⁵ proximately 74% by mass of this flux comes from ionized hydrogen (free protons), 18% from
¹⁰⁶ helium nuclei (two protons and two neutrons), and the remainder is trace amounts of heavier
¹⁰⁷ elements [1]. The majority of the cosmic ray flux observed at Earth is relativistic, in that the
¹⁰⁸ individual nuclei have kinetic energies greater than their rest mass ($E_k/mc^2 > 1$). The lower en-
¹⁰⁹ ergy cosmic rays (GeV-scale) are greatly influenced by the solar wind as well as the geomagnetic
¹¹⁰ field (see for example Fig. 1), which limits the flux interacting with the Earth. The high energy
¹¹¹ flux extends up to 10^{11} GeV at which point the cosmic ray loses energy from interactions with
¹¹² the cosmic microwave background. This is often referred to as the GZK cutoff¹ (GZK stands for

¹The highest energy cosmic ray observed was measured to have approximately 3×10^{20} eV[10] (48 joules), equivalent to a brick falling on your toe[11], all contained in a single proton, and later named the *Oh-My-God*

113 the initials of the three principle authors of the first theoretical prediction: K. Greisen [12] and
114 G. T. Zatsepin and V. A. Kuzmin [13]). The energy of the cosmic rays falls off rapidly with
115 energy: below 10^6 GeV, the flux falls off as $E^{-2.7}$, and above this it steepens to approximately
116 $E^{-3.1}$ [6]. For perspective, the number of 1 GeV cosmic ray protons is 8.1 orders of magnitude
117 higher than that at 1000 GeV (i.e. 2.7×3), or 16.2 orders of magnitude higher² than that at
118 10^6 GeV (i.e. 2.7×6).

119 When a primary cosmic ray collides with a nucleus in the upper atmosphere (typically with the
120 nucleus of an oxygen or nitrogen molecule), the energies can be large enough to break apart both
121 or either of the primary particle or the target nucleus through a nuclear interaction. Much of
122 the energy of the collision goes into producing short lived particles known as *mesons*³, the most
123 common being the π -meson or pion (π^+, π^-, π^0) and then the K-meson or kaon (K^+, K^-, K^0).
124 The charged pions (π^\pm) decay within approximately ten billionths of a second [16] producing a
125 same charge muons and a neutrinos (the charged kaons, K^\pm , are a bit more complicated, but
126 they also preferentially decay this ways as well, or to pions). The neutral mesons (π^0, K^0), decay
127 approximately one billion times faster (10^{-17} s) than the charged mesons, preferentially to gamma
128 rays. Unlike the neutral mesons, the charged mesons are able to travel far enough before decaying
129 to interact with another molecule in the atmosphere. This interaction in turn can be in the form
130 of another nuclear interaction (since mesons are made of quarks, they experience the strong
131 force responsible for the nuclear interaction), much like the original cosmic ray interaction. The
132 interaction may then produce even more mesons, contributing to the induced shower of particles
133 induced by the primary interaction. The primary cosmic rays do not penetrate directly to
134 Earth's surface due to the shielding provided by the atmosphere, however, a small flux of nuclear
135 fragments (such as protons and neutrons) from these interactions can occasionally cascade down
136 and make it to the surface. An illustrative diagram of a cosmic ray interaction is shown in Fig. 2.
137 The first interaction of vertical cosmic rays takes place at an altitude approximately between
138 15 km. Cosmic rays entering at an angle, will interact at higher altitudes due to their path
139 passing through more atmosphere[7].

140 The high energy photon from the decay of the neutral mesons quickly materialize into an
141 electron-positron pair, also referred to as *pair production*. These electron-positron pairs then
142 radiate high energy photons, which can again materialize into another electron-positron pair.
143 This electromagnetic cascade process continues, dividing the original energy of the photons be-
144 tween the numerous electrons, positrons, and lower energy photons at the end of the cascade.
145 Photons with energies less than 1.022 MeV, cannot further pair produce and will then their
146 interactions will be dominated by Compton scattering and photoelectric absorption. At lower
147 altitudes, there isn't a fresh supply of high energy neutral mesons due to the rapid decrease of
148 nuclear interactions.

Particle.

²The steep fall of in energy of the cosmic ray flux is why we require large detectors to measure the rare high energy events.

³Mesons are particles that, unlike the proton and neutron, contain only two quarks: one quark and one anti-quark. The lightest meson is the pion, then the kaon. There exists many other combinations of quark/anti quark pairs, however due to their higher masses, they are not preferentially produced and will not be discussed here. More information on this side of particle physics can be found in Ref. [14, 15]

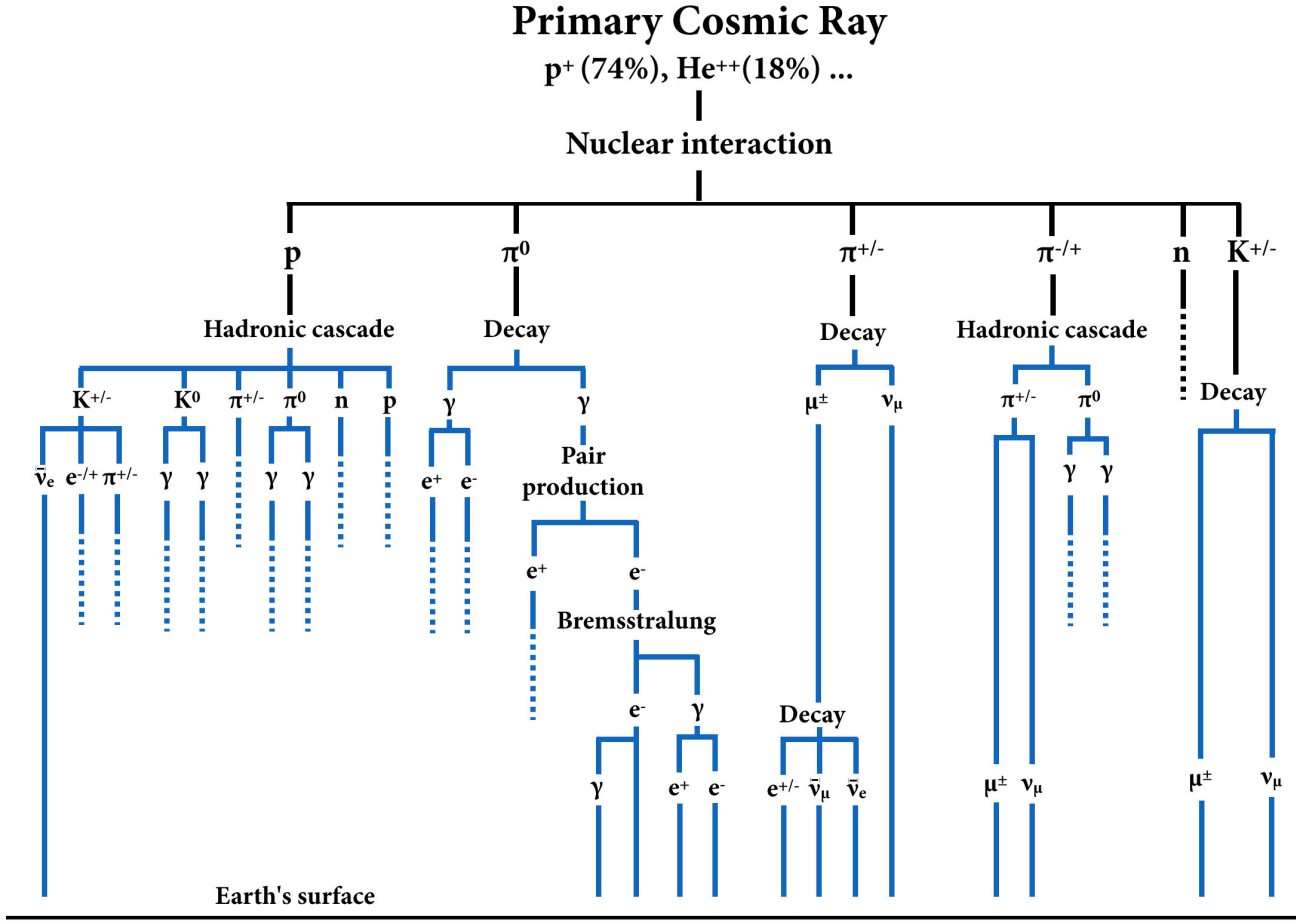


Figure 2: An schematic representation of the various decay and interactions chains that result from the interaction of a cosmic ray in Earth's atmosphere. This is a modified figure from Ref. [3].

149 The cosmic ray muons (μ^\pm) originate from the decay of the charged mesons. A charged pion will
 150 decay to a same-sign muon (and muon-neutrino) with a branching fraction of 99.98%, whereas
 151 a charged kaon decays to a muon (and muon-neutrino) 63.5% of the time [17]. The neutrinos
 152 are not electrically charged and only interact through the weak force, therefore they can be fully
 153 ignored in this discussion.

$$\begin{aligned} \pi^\pm &\rightarrow \mu^\pm + \nu_\mu (\bar{\nu}_\mu) \dots (99.98\%) \\ K^\pm &\rightarrow \mu^\pm + \nu_\mu (\bar{\nu}_\mu) \dots (63.5\%) \end{aligned} \quad (1)$$

154 Approximately 80-90% of the muon flux in the energy range of interest (GeV to TeV-scale)
 155 comes from the decay of pions, and the remainder from kaons[18]. The muons are particularly
 156 penetrating, that is, they essentially only interact through ionization as they travel through

atmosphere and other matter and can make it through a large amount of material. This is contrasted with *baryons* (particle comprised of quarks), which also interact through the strong force. This makes muons the most numerous charged particle showering down on the Earth's surface. Muons have a mass of 105.65 MeV and are also unstable particles with a half-life of 2.2×10^{-6} s. They decay to an electron and two neutrinos.

$$\mu^\pm \rightarrow e^\pm + \nu_e(\bar{\nu}_e) + \bar{\nu}_\mu(\nu_\mu) \dots (100.0\%), \quad (2)$$

however, again we can ignore the neutrinos. A cosmic ray muon with an energy greater than 2.4 GeV will be sufficiently relativistic that its half-life, as seen by an observer on the Earth, will be dilated enough to penetrate the atmosphere before decaying (in other words, the muon decay length becomes greater than 15 km – the approximate altitude of the cosmic ray muon production). Further, a typical muon will lose approximately 2 GeV of energy due to ionization as it passes through the atmosphere on its way to the ground. Combining these two facts with the fact that the geomagnetic field and interstellar solar winds drive back the GeV-scale cosmic rays, as well as the steeply falling cosmic ray energy spectrum, we can expect the average muon energy at Earth's surface to be greater than a few GeV. We typically quote the mean cosmic ray muon energy at Earth's surface to be approximately 4 GeV[1]. The muons that do not survive the journey to the Earth's surface decay. The resulting electrons (or positrons in the case of a μ^+), also referred to as *Michelle electrons*, contribute to the low energy electromagnetic component from cosmic ray showers at sea level.

Let us now compare the number of particles showering down on us at sea level. We'll limit ourselves to thinking about particles that are coming from one steradian about the zenith, this can be thought of as circular disk around the vertical (zenith) part of the sky whose area represents approximately $1/6^{th}$ of the total visible sky, or equivalently, a half-angle of 32° from the zenith. From this direction, we can describe the number of particles passing through a $1 \times 1 \text{ cm}^2$ horizontal surface per minute ($\text{cm}^{-2} \text{ min}^{-1} \text{ sr}^{-1}$) by following the measurements outlined in Ref. [1]. We expect approximately $0.4 \text{ cm}^{-2} \text{ min}^{-1} \text{ sr}^{-1}$ from μ^\pm with energies greater than 1 GeV; $0.2 \text{ e}^\pm \text{ cm}^{-2} \text{ min}^{-1} \text{ sr}^{-1}$ above 10 MeV, but the flux falls off fast with energy, becoming negligible above 1 GeV; and $0.0054 \text{ cm}^{-2} \text{ min}^{-1} \text{ sr}^{-1}$ from protons above 1 GeV; and a charged meson flux above 1 GeV two orders of magnitude lower than that of the proton flux. This means that the protons and charged mesons are insignificant at sea level, however, there is a significant muonic and low-energy electromagnetic component. In Ref. [5], the flux is divided into a hard component (essentially fully muons) which can penetrate 15 cm of lead, and soft component (approximately 60-65% muons and the remainder is electrons, positrons, and photons) which cannot. As we'll soon see, there are a variety of physical phenomena that influence fluxes, but the relative contributions listed here represent a useful approximation.

As we increase in altitude, the relative contribution from the ionizing radiation fluxes change. In particular, we see a larger contribution from both the protons and electromagnetic component, whereas the charged mesons are still sub-dominant. Once we pass the primary interaction region where the primary cosmic rays are most likely to interact (typically around 15-20 km), the secondary particles produced by the initial nuclear interaction die off and we see a decrease in the ionization radiation flux. The shape of the curve describing the ionizing radiation flux

197 as a function of altitude is called the Pfotzer curve, and where the ionizing particle production
198 reaches a maximum is termed the Regener-Pfotzer maximum [19].

199 **2.1.1 Flux variations due to solar system properties**

200 There are several properties associated with the interstellar medium that modulate the cosmic
201 ray flux, and in particular the observable cosmic ray muon flux. These properties are primarily
202 associated with behaviour of the Earth and Sun's magnetic field.

203 **The latitude effect:** Roughly speaking, the Earth has a magnetic field that behaves similarly
204 to a magnetic dipole orientated from north to south. The magnetic field points parallel to the
205 surface of the Earth near the equator, and perpendicular to the surface near the poles. Particles
206 traveling towards the Earth will be less deflected ($F=q\vec{v} \times \vec{B}$) near the poles compared to the
207 equator. Low energy charged particles passing through the magnetic field may even become
208 trapped in what's known as the *Van Allen radiation belt*. This presents a low energy cutoff,
209 where the magnetic field is able to deflect protons below approximately 10 GeV near the equator
210 (corresponding to a rigidity of 10 GV) and near 1 GeV at higher latitudes [20, 21].

211 **The East-West asymmetry:** The cosmic ray muon flux is larger looking towards the west
212 compared to the east due to the Earth's magnetic field. This is an effect produced by primary
213 cosmic ray particles being predominately positively charged. The positively charged muons
214 curve towards the east, meaning that the intensity from the west is stronger. This effect is more
215 evident in the upper atmosphere[5], and obviously a larger effect at the geomagnetic equator
216 than at the poles.

217 **Magnetic anomalies:** There are local geomagnetic field variations which causes a change in
218 the cosmic ray intensity. The most prominent being the *South Atlantic Anomaly (SAA)* [22],
219 which extends from the east coast Brazil to the west coast of southern Africa (-50.0 to 0.0
220 geographic latitude and from -90.0 to 40.0 longitude). This is the region where Earth's inner
221 Van Allen radiation belt extends closest to the planet's surface and provides the smallest amount
222 of protection from cosmic rays. In fact, the increased level of ionizing radiation when passing
223 through the SAA is responsible for radiation damage to electronics on-board Low-Earth Orbit
224 (LEO) satellites⁴.

225 **Solar modulation:** The observed cosmic ray flux at the top of the Earth's atmosphere depends
226 partially on solar activity which manifests itself as an 11-year cycle⁵. Solar winds can drive back
227 low energy cosmic rays entering the solar sphere and the modulation effect decreases with an

⁴The International Space Station (ISS) passes intermittently through the SAA [23] and has dedicated instrumentation for measuring the increased radiation dose to astronauts [24]. Astronauts from NASA missions as early as Apollo 11 [25] have also reported seeing flashes of light while being in orbit [27]. These flashes of light are attributed to high-energy particles in the space radiation environment, however many details on the origin are still unknown [26]

⁵There is also a 22-year cycle since the solar magnetic dipole flips polarity at every solar maximum, which occurs every 22 years [5]

228 increase in energy. According to Ref. [7], the 1 GeV cosmic-ray proton flux is twice as small
229 during maximum solar activity compared to minimum solar activity; similarly there is a 10%
230 reduction in the 10 GeV cosmic ray protons during the solar maximum.

231 **Solar Flares:** Solar-flares can eject protons with energies up to several GeV, the upper end of
232 which is able to produce muons through nuclear interactions. These events are rare transients,
233 and since the energy is low, it primarily has an effect on the low energy muon flux [28].

234 2.1.2 Flux variations due to atmospheric properties

235 Similar to the previous subsection, there exists terrestrial phenomena that also modulate the
236 cosmic ray muon flux.

237 **The Cosine Squared Law:** At greater angles from the vertical, cosmic ray muons must
238 travel through a much larger distance, and therefore amount of matter, to reach a ground-based
239 observer. A cosmic ray muon traveling vertically downwards may only travel through 15 km of
240 atmosphere, whereas one traveling in the horizontal direction must pass through approximately
241 500 km of atmosphere. The larger path length means that the muon will lose more total energy
242 due to ionization in the atmosphere and also have a higher probability of decaying before reaching
243 the ground. As a function of zenith angle, the cosmic ray muon intensity is expected to follow
244 a cosine squared dependence [1].

245 **The atmospheric attenuation:** Recall that the nuclear interactions between the primary
246 cosmic ray and atmospheric nucleus happen in the upper atmosphere. Therefore, particles
247 reaching sea level must have had sufficient energy to penetrate the remainder of the atmosphere.
248 An increase in atmospheric density (perhaps due to atmospheric pressure changes) will cause
249 secondary particles to lose more energy as they propagate to the Earth's surface. Due to this,
250 the muon rate turns out to be anti-correlated with the pressure (i.e. if the atmospheric pressure
251 increases, the cosmic ray muon rate decreases). The density of the atmosphere changes with the
252 season and therefore exhibits a time-dependence. From other measurements, this is expected to
253 be a percent level effect [29].

254 **The positive temperature effect:** To produce a muon, we require a charged meson to decay.
255 However, recall that the charged mesons are typically relativistic and have lifetimes on the
256 order of nanoseconds⁶. This gives the charged mesons sufficient time to potentially interact
257 with another nucleus in the atmosphere rather than decay. As the temperature increases, the
258 atmosphere becomes less dense and there are more particles to interact with and less chance
259 that they decay [30]. Rather than correlating this with the ground based pressure (as in the
260 paragraph above), it is more commonly correlated with atmospheric temperature – taking into

⁶For example, a 5-GeV π^\pm produced at 15 km will travel approximately 300 m before decaying. This distance is small compared to the interaction path length of approximately 13 km, which means that most charged pions will decay rather than interact. However, at approximately 115 GeV, the pion has an equal probability to interact or decay in the atmosphere.

261 account the temperature profile of the atmosphere. This effect is larger at higher energies and
262 therefore is typically measured in laboratories located deep underground where the low energy
263 cosmic rays have less of an influence [31, 32, 33].

264 **The negative temperature effect:** As the temperature of the atmosphere increases, the
265 atmosphere expands, moving the muon production region further out. This means that the
266 muon path length increases, which gives them a higher probability of decay prior to making it
267 to the ground. During the winter when the atmosphere is colder, shallower and more dense,
268 cosmic ray interactions happen closer to the Earth’s surface. The charged mesons quickly begin
269 to lose energy and have a less likely chance of decaying into muons.

270

2.2 Radioactive backgrounds

271 The previous section described the ionizing radiation that we expect from showers of particles
272 raining down from the upper atmosphere, and the expected phenomena that can modulate
273 this flux. This section will describe ionizing radiation that originates on the surface of Earth
274 and can also influence our measurements; we’ll refer to these as the *radioactive backgrounds*.
275 Radioactive backgrounds are sub-divided into primarily three main processes called alpha, beta,
276 and gamma radiation. Radioactivity is a quantum mechanical effect which is non-deterministic,
277 that is, we cannot predict when a particle will decay, rather we can only assign a probability to
278 it. The energy scale of these processes are relatively low (MeV-scale) compared to the energies
279 associated with the cosmic rays (GeV and above), but their natural abundance on the surface
280 of the Earth is sufficient that these are typically the dominant source of triggers in the Desktop
281 Muon Detector.

282 Alpha decay is the result of an unstable nucleus ejecting a helium nucleus (a bound state of two
283 protons and two neutrons), $(Z, A) \rightarrow (Z - 2, A - 4) + \alpha$. This is a quantum mechanical effect,
284 where a helium state (helium is a very tightly bound state) forms in the nucleus, then quantum
285 tunnels through the nuclear potential barrier, exiting the nucleus. The emitted alpha particle
286 is mono-energetic, and since the helium nucleus has a charge of $+2e$ and mass of approximately
287 4 GeV (therefore, it moves slow and has a large charge), it will lose energy rapidly in matter.
288 A 5-MeV alpha particle will have a range of 3.5 cm in air before losing all of its energy, or
289 equivalently, 23 micrometers in aluminum⁷ [34].

290 Beta radiation is described as the decay of a neutron to a proton⁸: $n \rightarrow p + e^- + \bar{\nu}_e$. The
291 proton remains in the nucleus, while the electron and electron-neutrino are ejected. Since this
292 is a 3-body decay, the electron is not mono-energetic. It is emitted with a continuous energy

⁷The high energy loss rate that alpha radiation makes it useful for cancer therapies. An alpha particle will deposit all of its kinetic energy into a very local space (order micrometers in human tissue), which is capable of destroying cancerous cells.

⁸More fundamentally, during neutron decays, a down-quark in the neutron converts to a up-quark, emitting a virtual W-Boson $u \rightarrow d + W \rightarrow d + e^- + \bar{\nu}_e$. On the macroscopic level, this appears as the transmutation of an atom converting to another atom with an extra proton and one fewer neutron: $A(Z, N) \rightarrow A'(Z + 1, N - 1) + e^- + \bar{\nu}_e$.

293 spectrum whose maximum energy is approximately at the total energy available for the decay
294 (the Q-value). Beta decays typically have energies that can range from tens of keV to a few
295 MeV.

296 Gamma radiation is simply a high-energy photon, emitted during the de-excitation of an atomic
297 nucleus. When the nucleus is in an unstable state (for example, maybe the nucleus absorbed a
298 neutron or was left in an excited state after a beta decay), it will de-excite into a lower energy
299 configuration releasing a photon. This is analogous to the de-excitation of an atomic electron,
300 emitting a characteristic mono-energetic photon. Since the energy levels in the nucleus are
301 quantized, gamma ray are also mono-energetic (with a small spread due to nuclear motion).
302 These energy scales are in the 100 keV to MeV-range.

303 3 Particle interactions with matter

304 In order to detect a particle, it must undergo an interaction with the material of a detector.
305 This section will go through the main interactions that transfer energy from the particle to
306 the absorbing material in sufficient detail to understand the data from the Desktop Muon De-
307 tector. We'll begin with the muons, protons, pions/kaons, and generically other high-energy
308 heavy charged particles, then move to high-energy electrons (and positron), and finally onto the
309 interactions associated with the radioactive backgrounds.

310 3.1 High energy heavy charged particles

311 The description below will be useful when thinking about any charged particles with a mass
312 much greater than that of the electron ($m \gg m_e$). This happens to be all charged particles
313 except for the electron and positron (e.g. the muon, the next lightest charge particle, is 206
314 times more massive than the electron). Unlike the trajectories of heavy charged particles, the
315 trajectories of electrons are not straight lines in a target and special consideration is required.
316 The description below represents an approximation to the underlying processes responsible for
317 energy loss in matter, since the breadth of this subject is far too large to cover in a single
318 document. More information can be found in Ref. [2, 9, 35, 36].

319 The energy loss rate (often called the stopping power), $-dE/dx$, is a measure of how much energy
320 is loss per unit distance traveled. It is often expressed in units of MeV cm²/g (referred to as
321 *mass stopping power*), where one simply has to multiply by the density (in terms of g/cm³) of
322 the absorbed to get the energy lost per cm. We've taken care of this by expressing the energy
323 loss rate in terms of water ($\rho = 1.0 \text{ g/cm}^3$), which coincidentally has approximately the same
324 density of plastic scintillator. As a particle travels through matter, it can be broken up into
325 three energy ranges that are mass dependent:

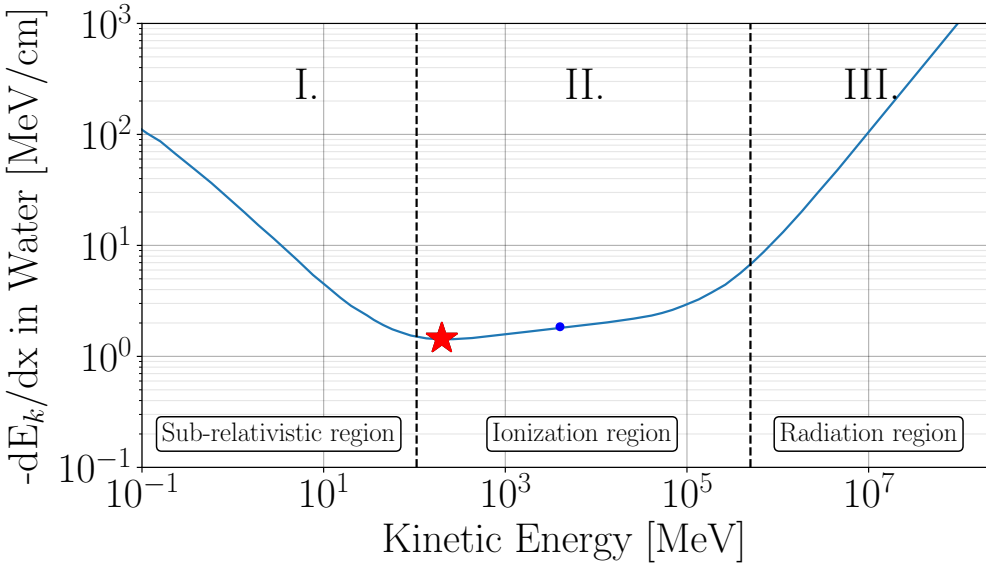


Figure 3: The kinetic energy loss per centimeter traveled, of a muon traveling through H_2O ($\rho = 1.0 \text{ g/cm}^3$). Modified from Ref. [16]. The blue dot represents the mean energy of the cosmic ray muons at sea level (4 GeV), and the red star represents where the particle is minimally ionizing.

- I. The sub-relativistic region: ($E_k < mc^2$)
- II. The ionization region: ($E_k > mc^2$ and $E < 400 \text{ GeV m}^2/\text{m}_{\mu}^2$)
- III. The radiation region ($E > 400 \text{ GeV m}^2/\text{m}_{\mu}^2$).

These three regions are shown in Fig. 3 for a muon traveling in water, however the energy loss can be scaled to another material by simply multiplying by the density (in g/cm^3) of the material (for example, the stopping power in lead would be scaled by a factor of 11.34). The energy loss can be scaled to another particle by multiplying by the charge of the particle squared. For example, the energy loss of an alpha particle will be scaled by a factor of 4. This plot is often represented in terms of momentum, but we've scaled it in terms of the kinetic energy of the incident particle to simplify the description. The vertical-dashed lines separate the three regions and can be scaled to another charged particle using the equalities above. For example, a proton will enter the sub-relativistic region at approximately 1 GeV.

In the **sub-relativistic region** (Muon: $E_k \approx 100 \text{ MeV}$; Proton: $E_k \approx 1 \text{ GeV}$), as the particle loses energy, the amount of energy loss per unit distance travels increases. Essentially, this means that once a particle enters this region, it comes quickly to a stop. This phenomena is also known as the *Bragg peak* [8].

In the **high energy radiation region** (Muon: $E_k \approx 400 \text{ GeV}$; Proton: $E_k \approx 27 \text{ TeV}$), the energy loss is associated with *bremsstrahlung*, pair production, and nuclear interactions, and

344 scales linearly with energy. The radiation term begins dominating at approximately 400 GeV
345 for muons, however, recall that the cosmic ray flux falls off fast with energy. The muons that
346 are in this regime represent a small percentage of the flux and lose energy fast.

347 Finally, the **ionization region** is where the majority of the cosmic ray muon flux lies. Recall
348 that the mean muon energy at sea level is 4 GeV (indicated as a blue marker in Fig. 3). The
349 energy loss in this region is due to ionization (breaking electromagnetic bonds) and excitation
350 (raise the electron to a higher-lying shell within the absorber atom) of the incident particle
351 and described by the *Bethe Bloch formula* (great descriptions of the formula can be found in
352 Refs. [8, 9, 16]). This region is particularly interesting since the energy loss rate is nearly
353 constant (it actually increases logarithmically), with an average energy loss rate of 2.2 MeV/cm
354 in a density 1.0 g/cm³ material, over many orders of magnitude. The minimum here, indicated
355 by a red star in Fig. 3, is where the muon is said to be a minimum ionizing particle (MIP) and
356 represents the energy at which the muon is most penetrating. The function is so flat in the
357 region of this minimum (up to approximately 400 GeV), that any particle whose energy is near
358 this red star is often called a MIP. It is also coincidental that the majority of the cosmic ray flux
359 falls into this region. This means that if we want to approximate the penetrating depth of a
360 typical cosmic ray muon, we can simply divide the energy by 2.2 MeV/cm and multiply by the
361 density of the absorber. As an example, a 10 GeV muon will penetrate through approximately
362 17 m of concrete ($\rho = 2.7 \text{ g/cm}^3$). What about the other heavy charged particles discussed in
363 this document: the protons, pions, and kaons? These will also lose energy through ionization,
364 but since they are composed of quarks, they can also interact via the strong force. The strong
365 force is responsible for the nuclear collisions that can greatly impact the particle and trajectory.
366 This is what makes the muons so unique – they do not interact via the strong nuclear force and
367 they are heavy, which allows them to penetrate through materials with minimal loses due to
368 collisions with the electrons in the absorbers and with minimal deflection on their trajectory⁹.

369 3.2 High energy electrons/positrons and photons

370 As described in Section 2.1, there is a non-negligible source of electrons/positrons with energies
371 below 1 GeV showering down onto the Earth’s surface. This section will describe the energy
372 loss in terms of high energy electrons, but the description is valid for positrons as well. It
373 turns out that for an electron above a few tens of MeV, the energy loss will be dominated
374 by radiation losses, predominantly *bremssstrahlung radiation* (“braking radiation” in German).
375 Bremsstrahlung radiation is the emission of photons produced by a particle accelerating and
376 decelerating as it passes near the electric field of the nucleus of the material.

377 A bremsstrahlung photon with sufficient energy can pair produce an electron and positron, which

9Since high energy muons are able to penetrate very large distances through material, many experiments are buried kilometers underground to shield against them. For example, the neutrino detector Super-Kamiokande, is buried underneath a 1-km mountain in Japan, in order to reduce the muon flux by a factor of 10^5 so that they are not swamped when looking for the rare, less energetic interactions from neutrino. For similar reasons, the IceCube neutrino detector is buried under 1.4 km of ice in the Antarctic glacier at the South Pole.

378 will subsequently radiate other bremsstrahlung photons, thereby creating a cascade of electrons,
 379 positrons, and photons. This process dominates the energy loss of the electron until the energy
 380 drops below a few tens of MeV (typically referred to as the critical energy). The radiation
 381 energy loss rate actually scales with energy, so in the region above the critical energy, dE/dx is
 382 proportional to energy. This means that a 20 GeV electron will start off by losing 1000 times
 383 more energy per centimeter traveled than a 20 MeV electron in the form of bremsstrahlung
 384 radiation. This causes the high-energy particles to lose their energy rapidly as a function of
 385 distance.

386 A *radiation length*, X_0 , is defined as the average thick-
 387 ness of a material that reduces the mean energy of the
 388 electron or positron by a factor $1/e$ (Euler's number =
 389 2.71828) due to bremsstrahlung radiation. This means
 390 that an electron will lose a factor of e^{-t} energy after
 391 traveling through t radiation lengths. For example, af-
 392 ter four radiation lengths, a 1 GeV electron will end up
 393 with approximately 20 MeV. A simplified model known
 394 as the *Heitler Model for electromagnetic cascades*, ap-
 395 proximates this saying that one electron-positron pair
 396 will be created per radiation length, each of which will
 397 receive half of the energy of the photon that produced
 398 them. After t radiation lengths, the cascade will con-
 399 tain 2^t particles (electron, positrons, and photons) each
 400 with an average energy of approximately $E = E_0/2^t$ [37].
 401 We've illustrated this in Fig. 4.

402 A useful list of radiation lengths for various materials can be found in Table 1. This table
 403 includes the information regarding pertinent materials used in the Desktop Muon Detectors or
 404 during some measurements below.

Table 1: A table of materials that are mentioned in this document and their corresponding radiation length. *STP indicates that the air is at the standard temperature and pressure: 20°C and 101.325 kPa. The data was collected from Ref. [1, 8].

Material	Density [g/cm ³]	Radiation length [cm]	Critical Energy [MeV]
Water (H ₂ O)	1.00	36.1	92
Lead (Pb)	11.35	0.56	9.51
Concrete	2.5	10.7	
Air at STP*	1.2931	30420	102
Scintillator (Polystyrene)	1.032	42.4	109
Aluminium (Al)	2.70	8.9	51.0

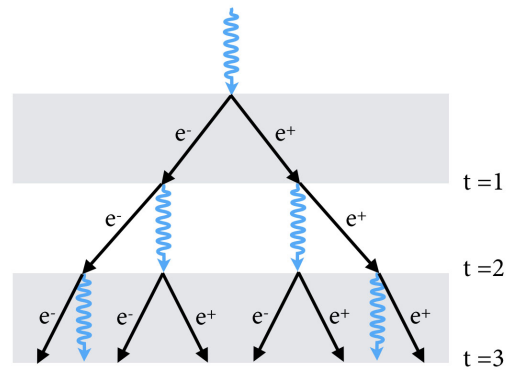


Figure 4: The Heitler Model for electromagnetic cascades.

405 3.3 Low energy electrons/positrons

406 Electrons and positrons are the lightest charged particles. The qualitative behavior for electron
407 scattering is different from the high-energy particles in two ways. First, the energy loss by elec-
408 trons fluctuates much more than for heavy particles. For example, the maximum transferable
409 kinetic energy of an electron from a 4 GeV electron is the full 4 GeV (since they have the same
410 mass), whereas a muon with the same energy has a maximum transferable energy of approxi-
411 mately 1 GeV. Further, because of its small mass, electrons are particularly susceptible to large
412 angle deflections by scattering off a nucleus. This probability is so high, in fact, that multiply
413 scattered electrons may be turned around in direction altogether, defined as *backscattering*. The
414 backscattering probability is higher at lower energies, and if backscattered, the electrons do not
415 deposit all their energy in the absorbing medium. A 1 MeV electron has approximately a 10%
416 chance of backscattering off of a thick slab of aluminium, and a 50% chance of backscattering
417 off a slab of gold [38].

418 The previous section described electrons and positrons with energy above the critical energy
419 of a material (typically tens of MeV), where their energy loss is completely dominated by
420 bremsstrahlung radiation. At lower energies, the electrons-positrons can in-elastically interact
421 through Coulomb collisions with atomic electrons to lose energy [39]. This leads to ioniza-
422 tion and excitation like the heavier particles. At lower energies still, MeV-scale, the electrons
423 (positrons) also exhibit *Møller (Bhabha)* scattering.

424 3.4 Low energy gamma rays

425 Gamma-rays interact slightly differently from the charged particles due to their lack of electric
426 charge. The three main interactions of gamma rays (and X-rays) are shown in Fig. 5.

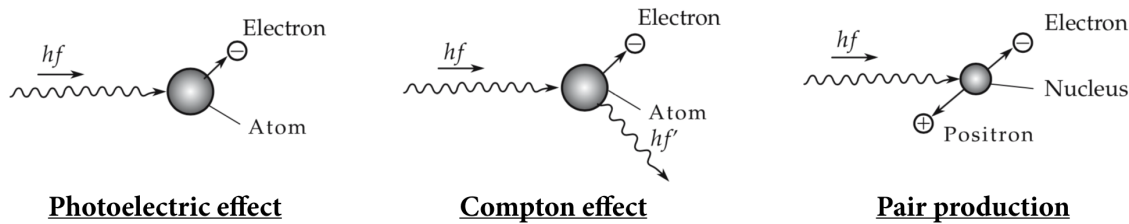


Figure 5: Modified from Ref. [34]

427 An atomic electron can fully absorb the energy of a gamma ray¹⁰, resulting in an electron
428 with the energy of the initial gamma ray (MeV-scale) minus the binding energy of the atomic
429 electron (eV-scale). This process is known as the *photoelectric effect*. As shown in Fig. 6,

¹⁰In order to conserve momentum, the photoelectric effect cannot occur on a free electron, it requires a nucleus to absorb part of the recoil.

430 the photoelectric effect dominates for low-energy gamma-rays with a moderate-to-high density
431 absorber.

432 *Compton scattering* results in the partial
433 transfer of energy from the incident gamma-
434 ray to an atomic electron, resulting in the elec-
435 tron being bumped into a higher energy level
436 or being ionized. The gamma-ray may change
437 direction, exiting the material that contained
438 the electron, or perhaps it scatters again off
439 another electron. Compton scattering domi-
440 nates at low energy for very low-Z materials,
441 and the probability of scattering will be pro-
442 portional to the electron density and therefore
443 proportional to the proton number of the ma-
444 terial.

445 At energies above 1.022 MeV, electron-
446 positron pair production plays a role. Pair
447 production follows the same description as
448 that found in the description on high-energy
449 electrons (Sec. 3.2). The only difference being
450 that the chain begins with a photon rather than an electron.

451 Beyond this, there are second order effects, such as *Rayleigh scattering* where the photon wave-
452 length is large enough that it coherently scatters off of the entire atom, and photonuclear inter-
453 actions at higher energies that break up the nucleus [16].

454 3.5 Neutrons

455 Like the photon, the neutron is not electrically charged, therefore it is not subject to Coulomb
456 interactions with the electrons and nuclei. Rather, it interacts through the strong force with
457 nuclei. Due to the short range nature of the strong force, these interactions are comparatively
458 rare (the neutron needs to get close to the nucleus in order to interact). Several interactions
459 that may occur are [8]:

- 460 1. Elastic scattering off a nucleus
- 461 2. Inelastic scattering off nucleus that leaves the nucleus in an excited state that may decay
462 emitting a gamma ray. To excite the nucleus the neutron must transfer MeV-scale energies.
- 463 3. Neutron capture. At low energies, the neutron might be captured by the nucleus, emitting
464 a gamma ray.

- 465 4. Fission
- 466 5. Hadronic shower, particularly at high energies (> 100 MeV).
- 467 High energy neutrons produced in the primary cosmic ray interaction, will often collide with
- 468 another nucleus creating a similar interaction as to the primary cosmic ray.

469 4 Detection methods

470 4.1 Single photon detections: photomultipliers

471 One of the most common instruments used by particle physicists are photomultipliers. Photomultipliers are devices capable of producing a measurable electrical signal from the interaction
472 of a single photon. Photon detection enables us to extract information related to the incident
473 particle by measuring the photon emission of a particle as it loses energy in a material. The
474 most prolific single photon sensing device is a photomultiplier tube (PMT), which offers a large
475 photo-sensitive area of coverage at modest cost. They are however bulky and require high-
476 voltage. Other common technologies, such as the Avalanche Photodiode (APD) and P-type and
477 N-type semiconductor photodiode (PIN photodiode), both have their benefits and drawbacks.
478 Recent improvements in the manufacturing of silicon chips have made it possible to make a
479 new type of photon detector called a *silicon photomultiplier*, or SiPMs (often abbreviated as
480 SPM). SiPMs have many advantages over PMTs, such as being able to operate at low voltages,
481 being insensitive to magnetic fields, being robust, and having a compact form factor. They are
482 also single photon detectors and have a peak responsivity near the peak emission from typical
483 scintillator. This modern technology is what we use in the Desktop Muon Detectors.

485 SiPMs are constructed out of densely arranged *microcells* (see Fig. 7), each of which is a separate
486 P-type and N-type semiconductor junction (P-N junction). When a P-N junction is first formed,
487 the free electrons from the N-type semiconductor diffuse towards the P-type semiconductor and
488 annihilate (similarly, the holes from the P-type diffuse into the N-type). Upon annihilation,
489 the boundary region between the P and N-type semiconductors becomes an insulator known
490 as the *depletion region*. When a photon travels through the depletion region, and deposits
491 sufficient energy to a bound electron, the electron can be transported to the conduction band,
492 thereby producing an electron-hole pair. If a potential difference is applied between the P-
493 N junction, the electron will gain energy and at a certain point collide with other electrons
494 also transporting them into the conduction band. When the potential difference is sufficiently
495 high ($> 5 \times 10^5 \text{ V/cm}$), an electron avalanche (or cascade) can occur (a Geiger discharge), in
496 which a single electron turns into a current of order millions of electrons. Once the flow of
497 electrons is initiated, the silicon becomes conductive at which point a quenching resistor lowers
498 the potential difference across the PN junction sufficiently to stop the electron cascade. In this
499 way, each microcell acts as a photon triggered switch which lets a small amount of current to

500 briefly flow if it was struck by a photon. The sum of the total current flow is proportional to
501 how many microcells were triggered and therefore is proportional to the incident photon-flux
502 (when the number of triggering photon ll number of microcells).

503 The Desktop Muon Detector employs the On Semiconductor MicroFC 60035 C-Series [40].
504 These are most sensitive in the 450 nm range [41], which is a deep blue to purple. If a photon
505 wavelength is too large (>1000 nm), the absorption length in the silicon is also too large and
506 the necessary size of the SiPM would be too bulky. If the photon wavelength is too short, it will
507 not penetrate into the sensitive region region of the SiPM, which is required for the detection.

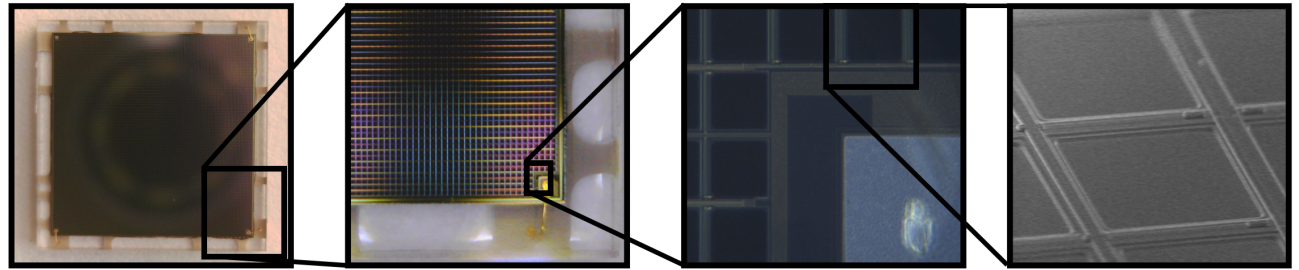


Figure 7: An image of a On Semiconductor MicroFC 60035 C-Series [40]. The SiPM has a length and width of 7.00 ± 0.05 mm and a thickness of 0.65 ± 0.05 mm. Each one of the tiled squares represents a single microcell, each of which operate independently in Geiger mode.

508 The applied potential difference is termed “bias voltage,” and dictates both how large of a region
509 is able to produce the avalanche (the depletion region), and the amount of energy gained by the
510 electron-hole pair. The “breakdown voltage” defines the voltage at which the voltage gradient
511 in the depletion region is large enough to create a Geiger discharge. This is typically between
512 24.2 and 24.7 V for the C-series SiPMs. If the bias voltage is increased beyond the breakdown
513 voltage, the microcells will still operate in Geiger mode, however the electron cascade in the
514 P-N junction will carry more energy, thus increasing the charge output (or gain) linearly. The
515 difference in the bias voltage to the breakdown voltage is termed *over-voltage*. An over-voltage
516 between 1.0 and 5.0 V is recommended. The Desktop Muon Detectors operate at an over-voltage
517 of 5.0 V which corresponds to a gain of roughly 5×10^6 [40].

518 Thermal fluctuations can produce electron-hole pairs, which mimic single photon events. For
519 our SiPMs, this occurs at rate of approximately 100 kHz per mm^2 , or at several MHz for the
520 full SiPM. This can be undesirable for many applications that rely on distinguishing between
521 small numbers of photons. The breakdown voltage required to initiate the electron cascade is
522 temperature dependent; a lower temperature has a lower breakdown voltage.

523 4.2 Scintillators

524 Scintillators are simply a material that absorbs energy (through Coulomb interactions) and re-
525 emits that energy in the form of electromagnetic radiation (scintillation light). Scintillators can

526 come in different forms: for example, the scintillator could be grown as a crystal (referred to
527 as an inorganic scintillator) with an added dopant, or the scintillator could have a fluorescing
528 material embedded in a plastic (such as polystyrene or acrylic) or mixed into a liquid (like
529 toluene or mineral oil) – these would be examples of organic scintillators. Inorganic scintillators
530 are typically more expensive, however they can also have a higher density and emit more photons
531 per unit energy deposited. This makes them more useful for calorimetry. Organic scintillators
532 on the other hand are typically cheaper since the fluorescent material is suspended in a common,
533 often low density material like a plastic, which enables them to be easily manufactured.

534 Scintillators are particularly useful since they emit light proportional to the energy deposited
535 in the material, therefore, one will often see a metric of the quality of the scintillator expressing
536 how many photons are emitted per absorbed MeV of energy (often called the scintillator
537 efficiency). A common organic scintillator may have an efficiency of 10,000 photons/MeV. An-
538 other important quantity associated with scintillators photon emission profile of the scintillator,
539 which determines what photon wavelengths are emitted after de-excitation. Scintillators must
540 also be transparent to the scintillation light so that it can propagate to the photon detector.
541 Plastic scintillators may have attenuation lengths on the order of 0.3 meters to 3 meters [42, 43],
542 whereas liquid scintillators like Linear Alkyl Benzene (LAB) can have attenuation lengths of up
543 to 25 meters [44]. Scintillators also have a very fast response and recovery (excitation and de-
544 excitation of the foreclosing molecules), which happens on the order of nanoseconds for organic
545 scintillators and hundreds of nano-seconds for inorganic scintillators.

546 The CosmicWatch Desktop Muon Detector was designed using an organic plastic scintillator,
547 which consists of a polystyrene base (essentially just an inexpensive transparent plastic) mixed
548 with a primary dopant of 1% by-weight of POP (2,5-diphenyloxazole) and 0.03% secondary
549 dopant POPOP (1,4-bis[2-(5-phenyloxazolyl)]benzene) [45]¹¹. This plastic scintillator does not
550 emit below 400 nm, and has a maximum emission around 420 nm (deep-purple light). This par-
551 ticular scintillator was developed by FermiLab for the MiNOS [47]/MINER ν A [48] experiments.
552 We'll focus on a description of organic scintillators below, but a good description of inorganic
553 scintillators can be found in Ref. [46].

554 The plastic scintillator requires three components:

- 555 • A transparent (in the visible spectrum) base that is used to suspend the fluorescent material.
556 This can be some sort of plastic (like polystyrene) or transparent liquid like mineral oil.
- 557 • A primary fluorescing agent that is excited by the energy transfer from the incident charged
558 particle. The de-excitation of the primary fluorescent material releases ultra-violet light.
559 Ultra-violet light will not travel far in the base (order mm), before being absorbed.
- 560 • A secondary fluorescent agent that absorbs the UV light and converts it to the visible
561 spectrum. The visible light then travels through the scintillator, internally reflecting off

¹¹Interestingly, PPO was one of the earliest compounds to be investigated as a scintillator solute by Hayes et. al (see Ref. [46]) from 1953-1958 and is still one of the most widely used

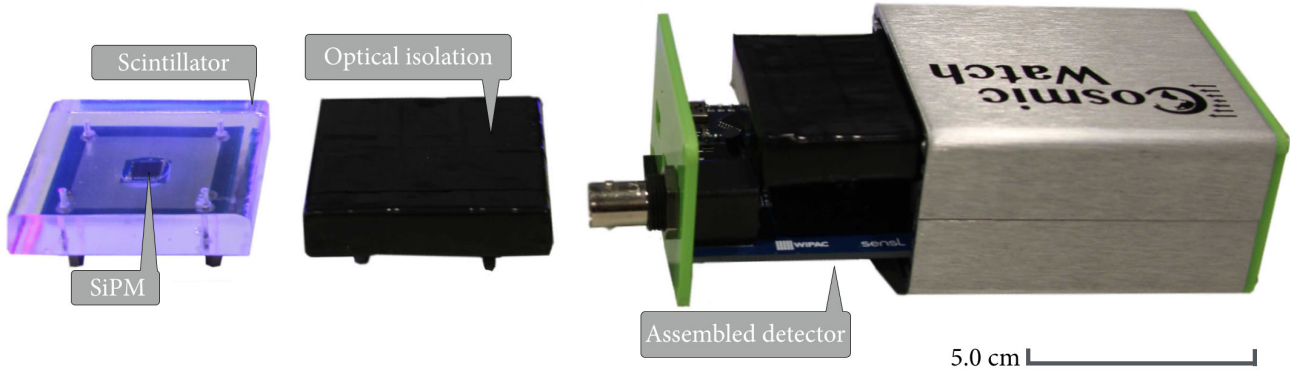
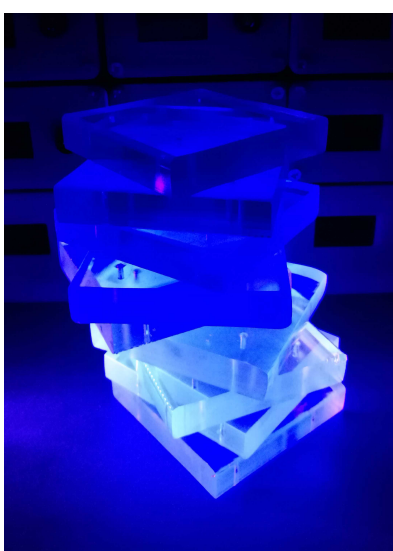


Figure 9: The components of the Desktop Muon Detector. Modified from Ref. [49].

562 the walls until it is absorbed. Some of the visible light will hopefully strike the photon
 563 sensor that is coupled to the scintillator.



571
 572
 573
 574
 575
 576
 577
 578
 579 Figure 8: A UV flash light
 illuminating scintillator.

564
 565
 566
 567
 568
 569
 570
 571
 572
 573
 574
 575
 576
 577
 578
 579 A simple illustration of the UV conversion is shown in Fig. 8.
 Here, we have illuminated several pieces of scintillator with a UV
 flash light. The UV is absorbed by the secondary fluorescent
 agent and re-emitted as a deep blue/purple light. Polystyrene-
 based scintillator has a density of roughly 1.032 g/cm^3 (similar
 to water) and a refractive index at standard atmosphere pressure
 of $n = 1.581$ [9].

The Desktop Muon Detector couples a SiPM (see Sec. 4.1) to a slab of scintillator via optical gel which reduces the probability of a photon being reflected at the interface by matching the index of refraction from the scintillator to the housing of the SiPM, eliminating the $n = 1.0$ air gap. We also wrap the remaining surface in aluminum foil to reflect photons that escape the scintillator. It is then wrapped in 2-3 layers of black electrical tape to make the whole thing light-tight. The assembly of a detector is shown in Fig. 9.

5 The CosmicWatch program

581 Many excellent programs exist to provide physics outreach expe-
 582 riences to students, and they each tend to offer very different opportunities and unique ideas.
 583 Recently, there has been quite a bit of interest in both the US (such as the Distributed Elec-
 584 tronic Cosmic-Ray Observatory, DECO [50]) and Poland-based (the Cosmic-Ray Extremely

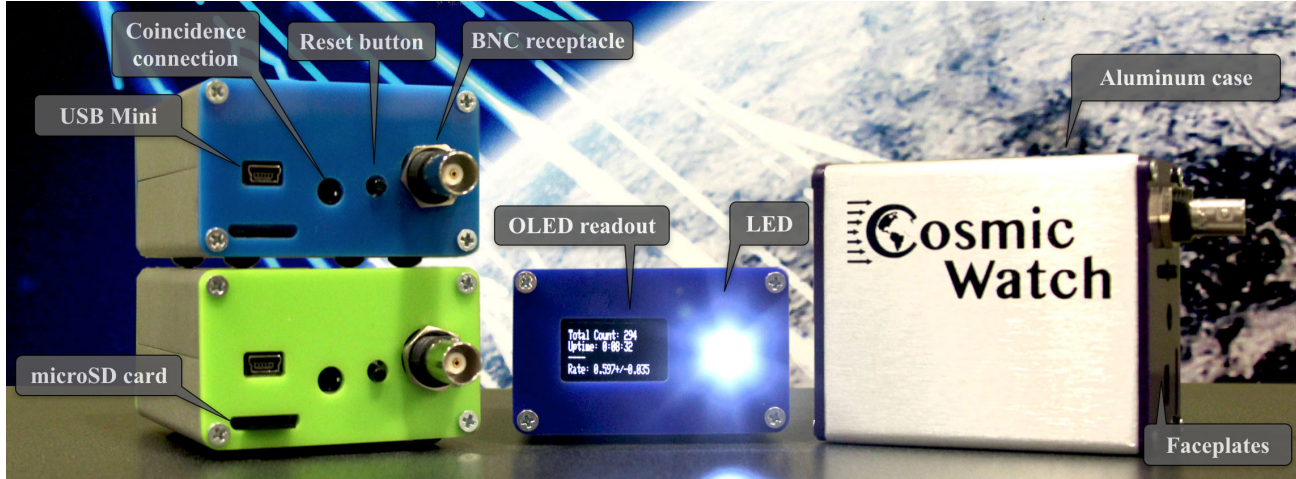


Figure 10: An array of Desktop Muon Detectors. From Ref. [49].

585 Distributed Observatory, CREDO [51]) cosmic ray programs that employs the CCD on a users
 586 smart phones to detect the interactions with cosmic-ray muons. We have also spoken with many
 587 people who work on the QuarkNet program [52], which brings elements particle physics to high
 588 school teachers using lab-grade muon detectors.

589 Our approach is slightly different than those mentioned above. The Desktop Muon Detector was
 590 designed to be as portable and self-sufficient as possible, while giving the individual student the
 591 ability to record and analyze their own data. The full detector is open source, and we encour-
 592 aged our students/teachers to go through the full build process themselves: acquiring materials,
 593 populating the circuit boards, troubleshooting the electronics, and finally testing the actual de-
 594 tector. This gives our students experience in the machine and electrical shop and introduces
 595 them to circuit design. Once the detector is built and functioning properly, students can either
 596 use our tools for analyzing the data, or they build their own programs for extracting physics
 597 from the data. The data is then used as an educational tool to illustrate various particle/astro
 598 physics phenomena.

599 5.1 The Desktop Muon Detector

600 Particle detectors in general aim to identify each particle, measure the energy and momentum,
 601 as well as localize the particle with sufficient resolution in space and time. A single detector is
 602 never optimal for all of these requirements. The CosmicWatch Desktop Muon Detector aims to
 603 be a general purpose detector that can collect granular information on these requirements such
 604 that it has access to a plethora of physics.

605 As described in Ref. [49], the CosmicWatch Desktop Muon Detector consists of a $5 \times 5 \times 1$ cm³
 606 slab of extruded plastic scintillator instrumented with a silicon photomultiplier (SiPM). When

607 a charged particle passes through the scintillator and deposits energy, some of that energy is
608 re-emitted isotropically along the particle track in the form of photons. Photons incident on the
609 photosensitive area of the SiPM can induce a Geiger discharge in the SiPM microcells. When the
610 microcells discharge, they produce a measurable current. A single photon can trigger a single
611 microcell (neglecting second-order effects), whereas multiple photons may trigger multiple cells.
612 The produced current is sent through a custom designed printed circuit board (PCB), which
613 amplifies and shapes the signal such that it is suitable to be measured by an inexpensive micro-
614 controller (in our case, an Arduino Nano [54]). The Arduino Nano measures the event time
615 stamp and peak value on the analog-to-digital converter (ADC). The measured peak ADC value
616 can then be converted back into a SiPM peak voltage, which is proportional to the number of
617 photons incident on the SiPM. If the measured ADC value is above a software defined threshold,
618 the micro-controller records the event data either to a microSD card or directly to a computer
619 through a USB connection. The CosmicWatch website also provides an online application to plot
620 data in real-time or to record data. For each event, the detector records the event number, event
621 time, average measured 10-bit ADC value, calculated SiPM peak voltage (which is proportional
622 to the SiPM pulse charge), total dead-time, and temperature. When plugged directly into a
623 computer, the data can be recorded through a python-based program that also includes the
624 computer time and date of each event.

625 An array of complete detectors is shown in Fig. 10. The front of the detector includes a built-in
626 0.96" OLED screen which displays the count number since the last reset, total uptime, count rate
627 (compensated for the detector dead-time), and an indication bar whose length is proportional
628 to the calculated SiPM peak voltage of the last triggered event. Multiple detectors can also be
629 linked together using a 3.5 mm male-to-male audio cable to make a *coincidence measurement*
630 (see Sec. 6.1). The detector was measured to draw 0.27 W and can be powered through any USB
631 connection (provided it supplies greater than 4.5 V). This includes the USB port on a computer,
632 USB power bank, or power outlet USB. The total mass of the detector, including the aluminum
633 case, is 178 g and the outer dimensions of the detector are 66.4 mm×101.6 mm×39.9 mm
634 (including the protruding BNC receptacle and LED holder). Excluding the aluminum enclosure
635 and end-plates, the detector has a mass of 76 g.

636 The backside of the detector includes a port for inserting and removing a microSD card; a USB-
637 mini port for powering the detector, uploading new code to the Arduino Nano, or recording
638 data directly through a USB port; a 3.5 mm female audio connection port used for connecting
639 multiple detectors together to make a coincidence measurement; a reset button used for resetting
640 the detector or assigning the detector as either the *master* or *coincident* detector in coincidence
641 mode (this will be described in Sec. 5.3.1); and a BNC connection which is connected directly
642 to the SiPM output, and can be used for injecting signals into the PCBs for testing.

643 The supplementary material pertaining to this project can be found in the GitHub repository
644 located in Ref. [55] and will be referred to as needed throughout. Included in the supplementary
645 material is a document (instructions.pdf) that describes the detailed process of building, testing,
646 and troubleshooting the detector.

647 5.2 Building and operating the detector

648 The detectors were designed to be as openly available as possible, and therefore we attempt
649 to use commonly available components all of which have been chosen to reduce the cost of the
650 detector. Occasionally, we find that the manufacturers of the components are out of stock,
651 so it is important for students to understand the provided information on the products we
652 use. The purchasing list (purchasing_list.pdf) found in the supplementary material includes
653 a detailed description of each components and where they can be purchased. Instructions
654 regarding purchasing the material and going step-by-step through a complete build can be
655 found in the instructions.pdf document, is located in the supplementary material.

656 We've also produced a set of YouTube [56] videos, in which we build a detector from scratch,
657 perform a simple measurement, then illustrate how to troubleshoot the detector. These can be
658 found here:

659 Introduction:

660 <https://www.youtube.com/watch?v=e4IXzNiNxgU>

661 Populating the Main PCB:

662 https://www.youtube.com/watch?v=zdVC8El_Xt8

663 Populating the SiPM PCB:

664 <https://www.youtube.com/watch?v=yFgin5wlw4I>

665 Troubleshooting:

666 <https://www.youtube.com/watch?v=Ck24HGrjBfY>

667 Beyond this, there are several pieces of software required to operate the detectors. They are
668 used for programming the Arduino and a python based program that we use for recording data
669 or plotting data in real-time on the website.

670 Regarding the Arduino, the supplementary material contains code used to program the Arduino
671 Nano (in the /Arduino directory). The code requires the user to download the Arduino IDE,
672 and install several libraries. A list of the libraries are found at the top of all the Arduino code
673 and within the installation instructions document. A description of the three pieces of code
674 follows:

- 675 1. **Naming.ino:** This code is used to permanently name the detector (permanent up until
676 this code is uploaded again). When this is uploaded to the Arduino, the variable, det_name,
677 is written to the EEPROM memory of the detector. It is recommended that every detector
678 is given a unique name.
- 679 2. **OLED.ino:** This code can be uploaded if the user would like information to print out on
680 the OLED screen.

681 3. **SDCard.ino**: This code sets the detector up to record the data directly to the removable
682 microSD card. If you are running this code, the OLED screen will not be updated.

683 Ideally, both the OLED.ino and SDcard.ino code would be contained in a single script, however,
684 due to the limited SRAM and flash storage on the Arduino, only one of the codes can be run
685 at a time.

686 Depending on the operating system that the student is using there may be special drivers needed
687 in order to get the Arduino Nano to communicate with their computer. In particular, when
688 using a Mac OS, the CH340g driver needs to be installed. This can be found in Ref. [57]. It's
689 best to try and simply get the Arduino Nano working on your computer prior to working with
690 the code above. Arduino provides an example code called Blink.ino, which simply blinks the
691 LED connected to Pin 13 at 1 Hz. Once this is working, it's simple to transition to our software.

692 The python code is used primarily for recording data directly to a computer, or to connect to the
693 website in order to plot the data in real-time. Recording the data directly to the computer has the
694 added benefit that the code will automatically add an extra time stamp to each event from the
695 computer. This gives an accurate time stamp to within approximately 1 ms. The python code,
696 import_data.py, can be found in the Recording_Data directory in the supplementary material.
697 In order to use the Arduino code, the user should have python 2.7 installed, and will have to
698 install two libraries:

- 699 1. **Tornado**: This library is used to communicate with the CosmicWatch server. On a Unix-
700 based machine, it can be installed through terminal using “sudo pip install tornado” or
701 through another package manager.
- 702 2. **Pyserial**: This is used to use python to read the data that is flowing into the USB port.
703 It can also be install through terminal using “sudo pip install pyserial.”

704 Once the libraries are installed, the import_data.py code can be run locally with python 2.7.

705 5.3 Recording data

706 Data can be collected from the Desktop Muon Detector in many ways:

- 707 1. **Through a microSD card**. To save data to a microSD card, the SDcard.ino Arduino
708 code must be uploaded to the detector and a microSD card (128 Mb is sufficient for all
709 applications in this documents) inserted into the port on the back of the detector. Each
710 time that the detector is reset or powered on, a new file is created with a file name that
711 count sequentially upwards from the previous file, and an “M” or “S” indicating if the
712 detector was in *master* or *coincident* mode respectively.

- 713 2. **Directly to a computer through a mini-USB cable.** To record the data directly to
 714 the computer, either the SDcard.ino or the OLED.ino code can be uploaded to the detector.
 715 When the detector is plugged into a computer USB port, and the import_data.py is run
 716 using python 2.7, the user is prompted to supply the path and name of the file to where
 717 the data is to be stored. It will then begin recording the data in real time to the output
 718 file. This method also includes a computer time and date stamp.
- 719 3. **Through the website.** Either the OLED.ino or the SDcard.ino code can be uploaded
 720 to the Arduino. When running the import_data.py code with python, there is an option
 721 to connect to the website (option: “Connect to server: www.cosmicwatch.lns.mit.edu”).
 722 After selecting this option, it will prompt the user to go to the website, where data from
 723 the detector will be plotted in real-time. At any point, the data can be saved in the form
 724 of a .txt file with the “save” button.
- 725 4. **Through the Arduino IDE.** When a detector is plugged into the computer, and the
 726 Arduino IDE is opened, the data can be seen accumulating in real-time in the serial
 727 monitor. The data can be copied and pasted into a text editor for later analysis.

728 When data is saved directly through the import_data.py script to the computer (either through
 729 method 2 or 3 above), the computer puts a time stamp with an precision and accuracy of +/-
 730 1 ms, that includes the computer date, computer time, and the detector name. An example of
 731 the data from the computer is shown in Fig. 11.

```
#####
### CosmicWatch: The Desktop Muon Detector
### Questions? saxani@mit.edu
### Comp_date Comp_time Event Ardn_time[ms] ADC[0-1023] SiPM[mV] Deadtime[ms] Temp[C] Name
#####
Detector ID: MrOrange
Detector Mode: Master
Data Service: Computer
2018-07-25 15:17:07.683137 1 5803 83 20.46 320 16.60 MrOrange
2018-07-25 15:17:08.374145 2 6493 512 144.44 358 16.71 MrOrange
2018-07-25 15:17:09.657944 3 7777 120 23.58 399 16.71 MrOrange
2018-07-25 15:17:11.481385 4 9602 143 25.74 471 17.14 MrOrange
2018-07-25 15:17:12.407065 5 10527 364 71.71 509 16.60 MrOrange
2018-07-25 15:17:14.232222 6 12352 271 46.93 583 16.92 MrOrange
2018-07-25 15:17:23.693371 7 21816 624 242.54 893 16.60 MrOrange
2018-07-25 15:17:24.210330 8 22334 332 61.17 934 17.14 MrOrange
2018-07-25 15:17:25.672181 9 23797 280 48.67 973 16.71 MrOrange
2018-07-25 15:17:25.979883 10 24103 335 61.77 1012 16.71 MrOrange
```

Figure 11: Example data format. The header for the file is the first 8 lines and 10 example events follow. This data was recorded using the detector named “MrOrange,” in *master* configuration, recorded directly to the computer through the import_data.py code. The definitions of the columns are listed in the header, as well as a more descriptive description in the text below.

732 The data shown in Fig. 11 is formatted into space delimited columns, each of which is labelled
 733 in the header, and defined as:

- 734 • **Comp_date:** The date given by the computer. Requires data saved using method 2 or 3
 735 from above.

- **Comp_time**: The time stamp given by the computer. Requires data saved using method 2 or 3 from above.
- **Event**: The event number of the detector.
- **Ardn_time [ms]**: The total elapsed Arduino time, measured in milliseconds. This is only accurate to roughly ± 1 min per day, and precise to the nearest millisecond.
- **ADC [0-1023]**: The ADC measurement for the event. The Arduino Nano has a 10-bit ADC, meaning the values reported are from 0-1023 (2^{10} values). The ADC is referenced between ground and 3.3 V using the internal Arduino voltage regulator.
- **SiPM [mV]**: The calculated SiPM peak voltage. This is a number calculated from the measured ADC value. It represents a number roughly proportional to the number of photons that triggered the SiPM. The conversion between the ADC value and the SiPM peak voltage is described in the calibration section of the instructions.pdf document.
- **Dead-time [ms]**: The total dead-time of the detector. This must be subtracted for any rate measurement from the elapsed time to determine the detector livetime.
- **Temp [°C]**: The measured temperature of the detector via the on-board TMP36 temperature sensor. Measured in degrees Celsius.
- **Name**: The detector name. The name is set using the naming.ino program. Requires data saved using method 2 or 3 from above.

When recording data to the microSD card using the SDCard.ino Arduino code, the **Comp_date**, **Comp_time**, and **Name** fields are omitted.

5.3.1 Setting detectors in master and coincidence mode

Many measurements in this document rely on the detectors operating in *coincidence mode* (e.g. see Sec. 6.1). This mode allows us to improve the purity of the cosmic ray muon sample by rejecting events that likely came from interactions from radioactive backgrounds. Coincidence mode requires two or more detectors connected together using a 3.5 mm male-to-male audio cable (I'll often refer to this as the *coincidence cable*). Once connected together, only one of the detectors requires power while the others are powered through the tip connection of the 3.5 mm cable. To set the detectors into the coincident configuration, simply reset the detectors while they are connected with the coincidence cable. The first detector to be reset becomes the *master* and the subsequent detectors, when reset within 10 ms to 2000 ms of the *master*, will become *coincident* detectors.

The master detector triggers on all events which create a pulse larger than the software defined threshold in the Arduino code. The coincident detector will only record events in which the master detector also triggered. These events are likely to be due to a cosmic ray muon, since the

770 backgrounds and accidental coincidence are unlikely to trigger both detector simultaneously. A
771 summary of why the purity of the cosmic ray muon signal increases when in coincidence mode
772 is below.

- 773 • Alpha particles will not penetrate a single detector (either the aluminum enclosure or even
774 the black electrical tape) and therefore cannot trigger both the master and coincident
775 detector at the same time.
- 776 • Beta particles can be significantly attenuated by the aluminum case, and have a significant
777 chance of scattering, thus losing energy. It's unlikely that the beta particle will be able
778 to deposit sufficient energy within the scintillator of the master, exit, then depositing
779 sufficient energy in the coincidence detector.
- 780 • Gamma rays can penetrate the aluminum enclosure and plastic scintillator, however they
781 have a significant chance of Compton scattering which will change the direction. If a
782 gamma ray does interact with both detectors, this means that it likely Compton scat-
783 tered off the scintillator slabs, lost sufficient energy to trigger the detector, then Compton
784 scattered or photoelectrically absorbed in the second detector, also depositing sufficient
785 energy to trigger the detector. This process is unlikely, and represents a small part of the
786 coincidence signal (an estimate of this rate is found in Sec. 6.7).
- 787 • Accidental coincidences from random events are unlikely. This will be elaborated on in
788 Sec. 6.
- 789 • A typical minimum ionizing muon passing through the slab of scintillator will typically
790 deposit more than 2 MeV of energy in the scintillator, without being deflected. If the
791 muon passes through both scintillators, it will likely trigger both detectors simultaneously.

792 Now that we understand how to build a detector, record data, and set up the detector into
793 coincidence mode, we can begin making measurements. The remainder of this document will
794 be dedicated to describing measurements we have previously made performed.

795 6 Example measurements

796 This section will describe a set of measurements made using the CosmicWatch Desktop Muon
797 Detectors (version 2) [49, 55]. This will be useful for those intending to use the detectors for edu-
798 cational purposes and students who are trying to make their own measurements. The individual
799 measurements below attempt to provide compelling evidence for the physical processes describe
800 in the first half of this document. Some of these measurements may be difficult for students
801 to perform, therefore we also provide the majority of the data and the scripts used to produce
802 these plots in the supplementary material. Reproducing these plots will require iPython to be
803 installed with a few extra libraries that are left up to the user.

804 When performing a measurement using the Desktop Muon Detectors, there are a few important
805 things to keep in mind.

806 1. The Arduino Nano is a relatively slow device, it is based off of an old processor called an
807 ATmega328P. Although this makes it cheap to purchase, it also means that there are subtleties
808 that we should be aware of. A critical aspect of any rate measurement performed with the
809 Desktop Muon Detector is that every command (such as adding two and two, or printing the
810 detector information to the serial port) takes time to perform. Accounting for the time that each
811 command takes is important since the detector is unable to trigger on an event if the detector
812 is busy. The term associated with the time we are unable to make a measurement is *dead-time*.
813 The dead-time is calculated in the Arduino code by measuring the time each command takes
814 in microseconds. This must be subtracted from the up-time in order to accurately calculate the
815 time that the detector was able to make a measurement; the result is called *live-time*. Dead-time
816 is a common feature in all particle physics detectors, however for us it is particularly important
817 due to the limited speed of the Arduino.

818 2. The detector orientation of the master and coincident when making a measurement will
819 have different characteristics. When making a coincidence measurement, it is important to
820 think about what is being measured, and how the orientation will effect the measurement. For
821 example, if we are interested in the angular spectrum of cosmic ray muons, we want to only
822 accept muons coming from a small solid angle. Fig. 12 shows several possible configurations
823 that are used in this document. The left side of Fig. 12, labeled as (a), shows two detectors
824 spaced a few centimeters apart and connected with a coincidence cable. We see that only the
825 muons that travel downwards through the blue area are able to trigger both detectors. Whereas
826 Fig. 12 (d) will trigger on muons that come in over a large solid angle.

827 3. Two independent events could have triggered both the master and coincident detector acci-
828 dentally if they happened to arrive within the coincidence time window. This becomes much
829 more likely at higher count rates. If we assume that the individual count rates are determined
830 by Poisson statistics, and that the two detectors are independent, then the probability of ob-
831 serving n events when the mean number of events is expected to be μ , is given by the Poisson

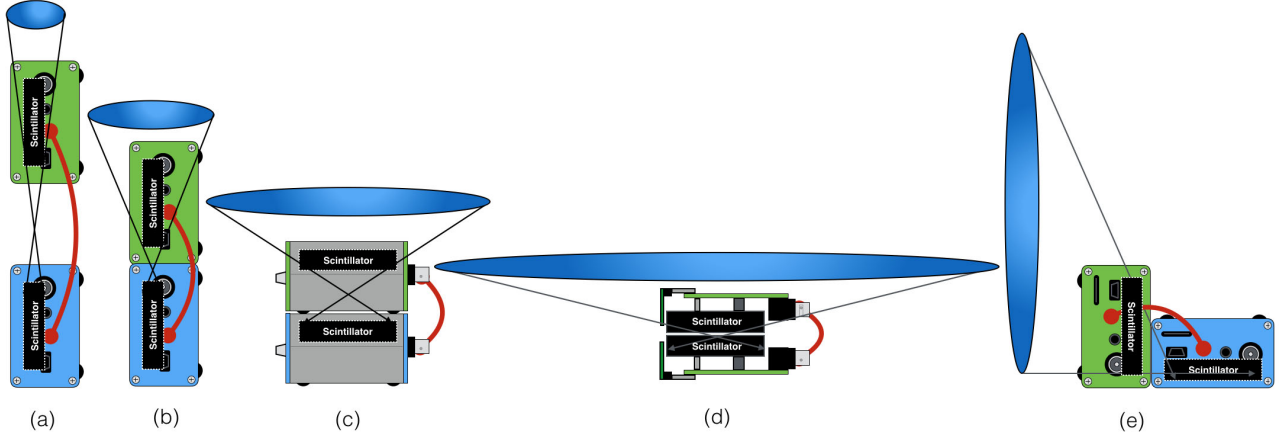


Figure 12: This figure shows several configurations for setting up the detectors in coincidence mode. Moving from left to right the solid angle subtended between detectors increases (illustrated as the blue ovals above the detectors) as well as the coincidence rate as measured by the coincident detector.

832 distribution:

$$f(n, \mu) = \frac{\mu^n e^{-\mu}}{n!} \quad (3)$$

833
 834 Following Ref. [9], let the count rate on the two detectors be N_1 and N_2 , and the coincidence
 835 window (the time window in which an event will be labeled as a coincident event) be τ . The
 836 average count rate for both detectors at sea level is approximately 1 Hz, and given a coincident
 837 time window of roughly $30\mu\text{s}$, we expect on average 0.000030 events in the time window ($N_{1,2} \times \tau$).
 838 Therefore, the probability of observing zero event in the time window is $f(0, 30 \times 10^{-6})$ and the
 839 probability of one detector observing an event in the coincident time window is $1 - f(0, 30 \times 10^{-6})$.
 840 Since the second detector could have also triggered first, then the rate of accidental triggers is:
 841 $R = 2N_1 N_2 \tau$. This corresponds to an accidental coincident rate for two detectors of 1 every
 842 15,000 events, or roughly six events per day using two detectors.

843 More generally, assuming that there are q detectors, each with the same baseline count rate N ,
 844 then the number of p -fold coincidence out of q detectors is:

$$R_p(q) = \binom{q}{p} p N^p \tau^{p-1} \quad (4)$$

845

846 6.1 A coincidence measurement

847 A coincidence measurement refers to a measurement in which we have extracted only the events
848 which have triggered multiple detectors within some time window. The time window when using
849 the 3.5 mm coincidence cable is approximately $30\mu\text{s}$. The implementation of this isn't obvious
850 when examining the Arduino code. It works by having the master detector immediately send
851 Pin 6 on the Arduino HIGH, each time it registers an event. The detector in coincidence mode
852 has its pin 6 set-up as an input. The 3.5 mm coincidence cable connects Pin 6 on both detectors
853 together through the ring terminal. When the coincidence detector registers an event, it first
854 waits approximately $30\mu\text{s}$ before checking to see if the Pin 6 is HIGH; if the pin is HIGH, it counts
855 the event, otherwise the event is dropped. The time window was chosen to accommodate the
856 slow ADC sampling time. A single ADC sample takes approximately $10\mu\text{s}$ (we've increased the
857 sampling speed using a *pre-scaler* in the Arduino code), which means that the master detector
858 may have triggered up to $10\mu\text{s}$ after the coincidence detector. Note that since the time window
859 is so large, we cannot determine which detector actually triggered first (a relativistic particle
860 will travel 9 km in $30\mu\text{s}$), therefore it doesn't matter if the coincidence detector is on-top or
861 below the master detector.

862 Typically, when a detector is placed
863 in coincidence mode, only the coincident
864 events are saved. For this measurement
865 however, we slightly modified the Arduino
866 code such that both the coincident and non-coincident
867 events are saved, and we label each
868 event to indicate what type it was.
869 Two detectors were placed into configura-
870 tion (d) of Fig. 12, and connected via a 3.5mm
871 coincidence cable. The calculated SiPM pulse
872 amplitude for this data set is shown
873 in Fig. 13. We see that the two
874 data subsets (coincident versus non-
875 coincident events) populate different
876 regions. This is due to the discussion
877 found in Sec. 3.1 and 5.3.1

880 In areas of high radioactive backgrounds, the non-coincident events may dominate the spectrum
881 even at 50 mV. The width of the peak shown in the coincident events at a SiPM peak voltage
882 of 50 mV can vary depending on how well the detector was built. For example, if the coupling
883 between the SiPM and scintillator was poor, the SiPM will observe fewer photons per event thus
884 reducing the resolution of the detector.

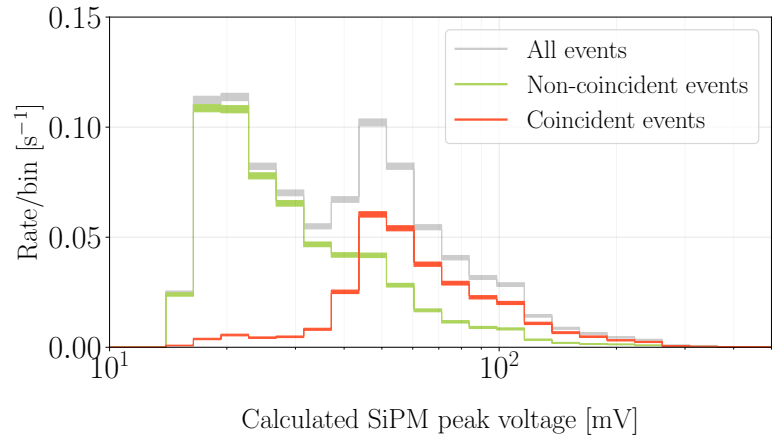


Figure 13: A coincidence measurement showing the calculated SiPM pulse amplitude for the coincident events and non-coincident events.

6.2 Measuring the cosmic ray muon rate in an airplane at 33,000 ft

A rate measurement was performed during a flight from the Boston International Logan Airport (BOS, latitude = 41.8°) to the Chicago O'Hare Airport (ORD, latitude = 41.8°) using a single detector. The data was recorded to a microSD card with and plugged into a 10,000 mAh USB power bank. The altitude of the airplane was collected from the flight records found in Ref. [58].

Fig. 14 (left) shows the trigger rate of the detector in blue as a function of time, binned into 60 second intervals. The error bars shown here are purely statistical. The altitude data of the airplane was linearly interpolated between points to estimate the altitude at any given minute. The interpolated altitude data was the fit to the detector data using a simple exponential plus an offset. Since we did not know the absolute take-off time (data was recorded to the microSD card), we allow the altitude time stamps to shift during the minimization. The best-fit equation is shown at the top left of this figure, where $\text{ALT}[t]$ represents altitude measured in kilometers as a function of time. The best-fit is also plotted in dashed red.

Fig. 14 (right) shows the measured trigger rate as a function of true altitude. Here, we show the exponential fit extended beyond the measured values. The count rate uncertainties were calculated by taking the square root of the sum all the events measured at a particular altitude. One thing to note is that this is data taken with a detector in master mode, which means it is also sensitive to the background radiation from the interior of the plane.

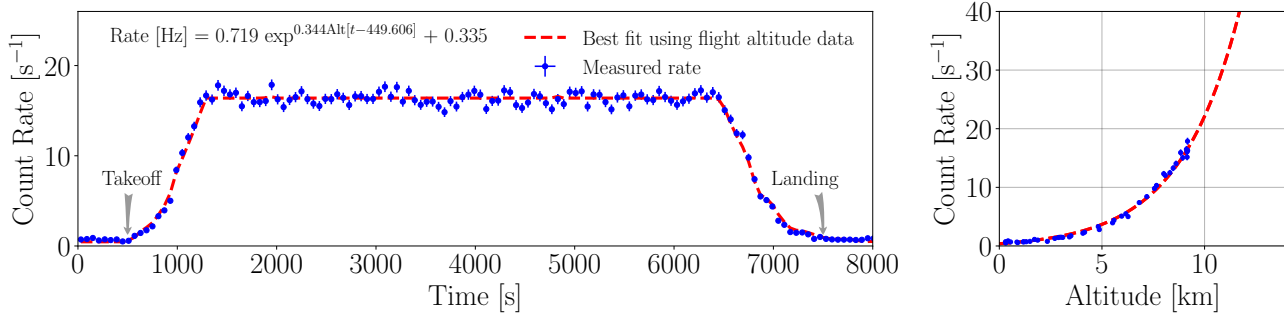


Figure 14: (Left) The count rate measured during a flight from Boston to Chicago as a function of altitude. The red-dashed line shows the actual amplitude of the airplane [58] scaled by a fitted exponential shown at the top left of the plot. (Right) The count rate as a function of altitude.

The cosmic ray muon flux is known to vary also as a function of latitude, which we have avoided by measuring the flux at a near constant latitude. We also expect the exponential fit to fail as we extend to higher altitude, due to the change in flux composition near the primary cosmic ray interaction region.

907 **6.3 High altitude balloon measurement at 107,000 ft**



Figure 15: An image from the high-altitude balloon flight at 107,000 ft. Photo from *Daniel Kaczmar - DNF Systems*.

908 As noted in Sec. 2.1, primary cosmic rays interacting
909 in the upper atmosphere produce showers of
910 particles, some of which decay to muons. Muons
911 are typically produced near an altitude of 15 km.
912 At higher altitudes, there is an increase in the con-
913 tribution from other ionizing particles, primarily
914 from electrons/positrons, and protons.

915 During the NearSpace2018 conference [59] in Torun
916 Poland, we participated in a high-altitude balloon
917 (HAB) flight to measure the ionizing radiation flux
918 as a function of altitude. Two detectors were used
919 for the flight so that we could measure both the to-
920 tal rate on the master detector and the down-going
921 rate on the coincident detector. The detectors were
922 placed one-on-top of another (configuration (d) in
923 Fig. 12) and taped together to ensure their ori-
924 entation relative to each other remained the same
925 throughout the flight. The BNC connectors and
926 the OLED screens were removed from the PCB to
927 reduce the weight. An 8" 3.5 mm audio cable was used to connect them into coincidence mode
928 and the SDCard.ino code was uploaded to both detectors. An image of the two detectors is
929 shown in Fig. 16. Both detectors were powered by single cell lithium ion battery.

930 The temperature during the ascent was expected to reach -60°C , therefore thermal protection
931 was required both for the battery and in order to minimize the effect on the SiPM described in

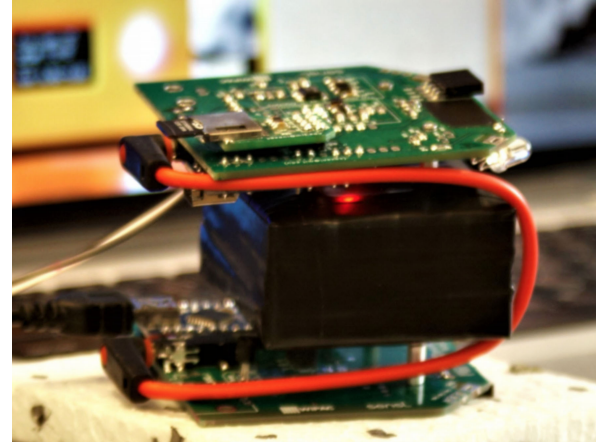


Figure 16: The two detectors flown in the HAB flight. The scintillators were taped together in order to preserve the detector orientation relative to each other.

932 Sec. 4.1. A $10 \times 10 \times 10$ cm 3 Styrofoam enclosure was constructed with a wall thickness of 1 cm,
 933 to house the components. This was sufficiently large that we could place the two detectors and
 934 a small heating element in the enclosure with two single-cell Lithium-ion batteries (one to power
 935 the detectors, and the other to power the heater). A micro-switch was connected to the battery
 936 and wired outside the enclosure so that we could power on the detector just prior to the flight.

937 The HAB was launched on September 22nd, 2018 at 12:53 pm. DFN System recorded the
 938 balloon altitude and location using on-board GPS, they also mounted a camera to the balloon
 939 that looked down at the payloads, an image near the maximum altitude of the flight is shown in
 940 Fig. 15. The master (orange) and coincident (green) detector count rate, binned in to 60 second
 941 intervals, is shown in Fig. 17, along with the altitude data from the GPS (black).

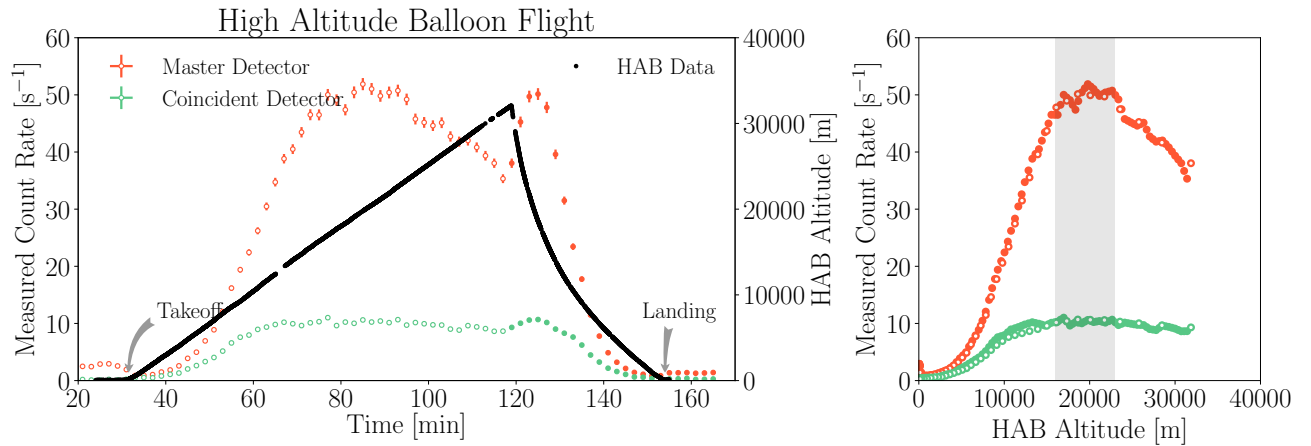


Figure 17: (Left) The measured trigger rate for the master (orange) and coincident (green) detector during the high-altitude balloon flight. Take-off occurred 30 minutes after powering on the detectors. The black data points correspond to the altitude as measured through the on-board GPS. (Right) The GPS altitude as a function of trigger rate. The uncertainty in both these plots are statistical.

942 The shape of the measured spectrum in Fig. 17 corresponds to the Pfotzer curve. We find an
 943 initial maximum count rate (Regener-Pfotzer maximum) for the master detector at an altitude
 944 from approximately 16-23 km approximately 70-95 minutes into the measurement. After the
 945 balloon popped (at minute 118), the detectors fell through the Regener-Pfotzer maximum. The
 946 decrease in the trigger rate after passing the maximum occurs due to the detectors ascending
 947 beyond the primary interaction region.

948 The coincidence detector shows a flatter maximum at an altitude from approximately 12-25 km.
 949 The peak begins at lower altitudes since we are now preferentially triggering on vertically down-
 950 going particles. As described in Sec. 2.1.2, primary particles entering the Earth's atmosphere
 951 at larger angles from the zenith will interact at higher altitudes. In agreement with the data.



Figure 18: Leaving McMurdo Station, Antarctica on a C-130 Hercules for the South Pole Station.

952 6.4 Muon rate measurement while flying to the South Pole

953 In December 2018, I flew to the South Pole as part of a field team to perform maintenance and
 954 upgrades on the IceCube Neutrino Observatory [60]. During the flight I measured the ionizing
 955 radiation with two detectors orientated in configuration (d) of Fig. 12. Data was recorded to
 956 the microSD cards and powered through a single 30,000 mAh power bank.

957 The first four flights (from Madison, WI USA to Christchurch, New Zealand) were operated by
 958 United Airlines and New Zealand Airlines. The altitude data was publicly available for these
 959 flights on FlightAware.com [58]. The flight leaving from Christchurch New Zealand, to McMurdo
 960 Antarctica, was on a C-17 military jet operated by the US Air Force. Similarly, we flew on a
 961 C-130 Hercules, the day after to the South Pole. Since these were military flights, the altitude
 962 of this flight was not available; however, several altitude measurements on the second flight
 963 were made using GPS. We landed several days later on the 2700 m thick South Pole glacier,
 964 approximately 0.5 km from the actual Geographical South Pole.

965 The full master and coincident detector data are shown in Fig. 19, with descriptions of each
 966 flight in the text boxes. To give perspective for other measurements, the total data collected
 967 by the master detector was about 50 Mb, whereas the coincidence detector was approximately
 968 15 Mb.

969 Fig. 19 illustrates a several very interesting properties. First, there is a trend towards lower
 970 count rates near the equator. This is due to the latitudinal variation in the cosmic ray flux

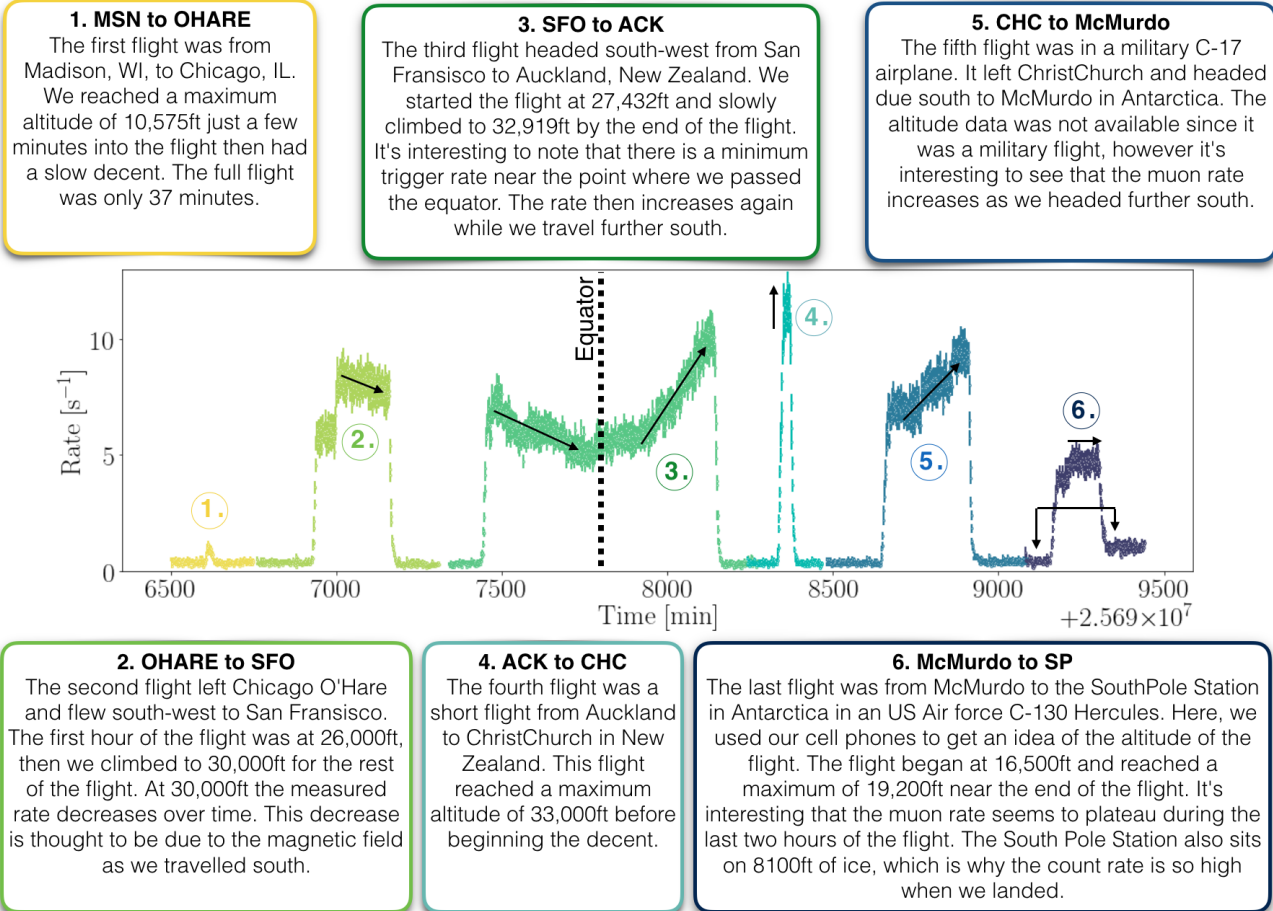


Figure 19

described in Sec. 2.1.2. This effect is most obvious in the flight from SFO to ACK, which traveled at nearly a constant altitude and a constant rate of latitude change from $+32^\circ$ to -32° . We see that the rate is not symmetric. This is because the magnetic latitude is offset from the geographical latitude, which in turn is because the magnetic field is not symmetric about the equator. Second, it's interesting to see that when we landed at the South Pole, there is a noticeable change in trigger rate due to the combination of the elevation and change in Earth's magnetic field.

While flying through the equator at 35,000 ft, I performed an East-West measurement using configuration (e) of Fig. 12. We measure a count rate coming from the east of 0.69 ± 0.02 cps, while from the west 0.84 ± 0.03 cps. This represents a $22.2 \pm 7.4\%$ increase in the westward direction. This east-west asymmetry is described in Sec. 2.1.2.

982 **6.5 Latitude correction to the cosmic ray muons**

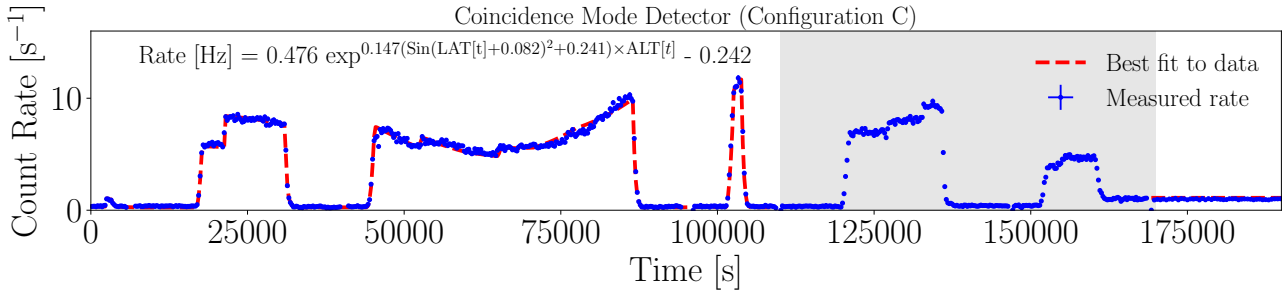


Figure 20: The fitted data based on the altitude and latitude data from the first four flights. The fit also includes a measurement after landing at the South Pole, where the altitude and latitude were known (2700 m and -90°). The two military flights were not included in the fit.

983 We observed latitudinal variation in the cosmic ray
984 muon rate in the previous measurements. This was
985 an expected effect due to the change in the Earth's
986 magnetic field as a function of latitude. Here, we
987 will empirically attempt to account for the varia-
988 tion in the latitude and altitude based on the pre-
989 vious measurement. We will assume that the change
990 in the rate as a function latitude follows a sine-
991 squared form; where the minimum occurs near the
992 equator and the maximum occurs near the poles:

$$R[\text{Hz}] = N \exp^{\alpha(\sin(\text{LAT}[t]+\theta)^2+\beta) \times \text{ALT}[t]} - b \quad (5)$$

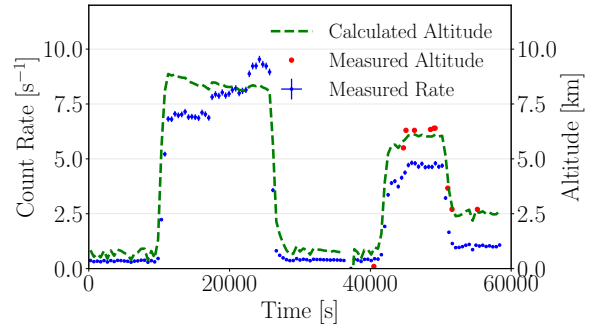


Figure 21: The measured muon rate along with the calculated flight altitude in green. Red shows the few measurements made on the actual altitude..

993
994 Here, θ represents a phase that offsets the latitude
995 to account for the difference between the geographical latitude and the magnetic latitude, β is a
996 factor that permits an altitude effect at the magnetic equator (set the sine term to zero), α is a
997 scale factor that dictates the strength of the latitudinal and altitude effect, N is a normalization
998 that sets the scale for the exponential component, and b is an offset that accounts for a constant
999 background radiation.

1000 Fig. 20 uses the function in Eq. 6.5 to fit the data for the first four flights, plus the data after
1001 landing at the South Pole. The best fit values are shown at the top left of Fig. 20. Using this
1002 result, we can then invert formula Eq. 6.5 to calculate the altitude of the two military flights
1003 (assuming we flew at a constant velocity directly south). The calculated altitude is shown in
1004 Fig. 21 for the military flights in green, as well as the measured altitude from GPS in red.

1005 6.6 Cosmic-ray muon rate at various locations on Earth

1006 Acquiring data at different elevations above sea level can be challenging since many locations
 1007 do not have immediate access to large changes in elevations. During 2018, we recorded the
 1008 muon rate at various locations on the planet that we visited. Each measurement was performed
 1009 in configuration (c) of Fig. 12 using the coincidence connection, and all data was recorded
 1010 to the microSD card. The altitude data of each location was found through Google and not
 1011 corrected for changes due to geological features or the altitude of the measuring location (future
 1012 measurements will use GPS to give a more accurate altitudes). The exceptions in this data set
 1013 are the cases of the trans-Atlantic flight and the HAB measurement, whose altitude data was
 1014 found using FlightAware.com and GPS respectively. Fig 22 shows the measured count rate at
 1015 various locations (the trans-Atlantic flight data was recorded at an altitude of 33,000 ft and
 1016 high-altitude balloon measurement was taken from the Pforzheim maximum described in Sec. 6.3).

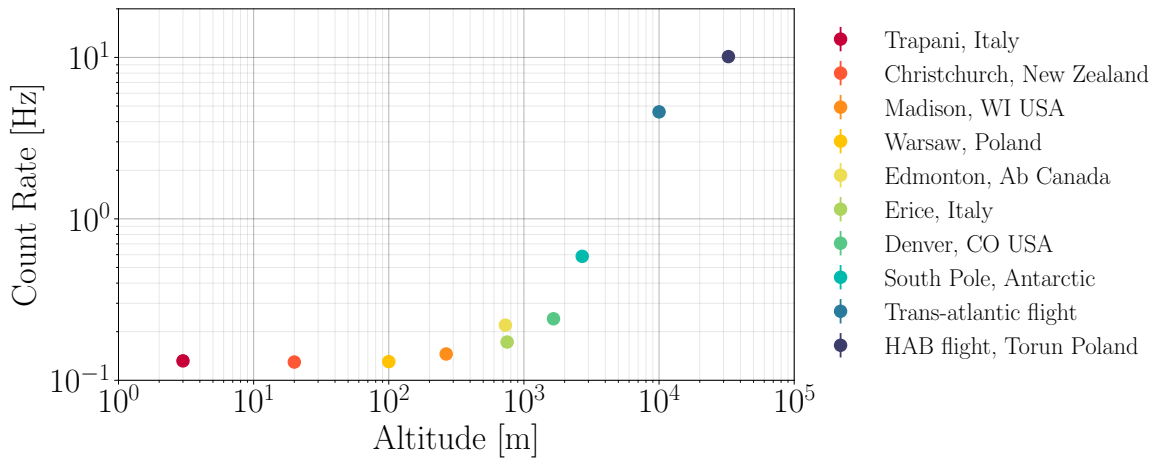


Figure 22: The coincident detector count rate at various locations throughout the world. The trans-Atlantic flight rate was measured at 30,000ft, while the high-altitude balloon data was simply the count-rate at the Pforzheim maximum described in Section 6.3. The statistical error bars of each point are smaller than the marker size.

1017 As expected, at higher altitudes, we observe a statistically significant change in the measured
 1018 count rate. An interesting exception is noted when comparing the measurement at Sherwood
 1019 Park, Alberta Canada, versus Erice, Sicily Italy. They are both at approximately the same
 1020 the same altitude and latitude, however there is a 27% measured rate difference between the
 1021 two. This is thought to be due to the electromagnetic component of the shower not being
 1022 properly shielded in the measurement in Canada. The Erice measurement was performed in a
 1023 large concrete tower with several concrete floors above the detectors, while the measurement in
 1024 Canada was performed on the ground floor of a two story wooden house. The lack of shielding
 1025 against the electromagnetic component of the atmospheric flux is thought to be the primary
 1026 source of this discrepancy.

1027 **6.7 Rate measurement 1 km underground at Super-Kamiokande**



Figure 23: Dr. Katarzyna Frankiewicz floating in the inner detector of Super-Kamiokande during the Gadolinium upgrade 2018.

1028 Two Desktop Muon Detectors were brought to the Kamioka Observatory located 1 km under-
1029 ground in the Mozumi Mine, Japan. This mine is home to several high profile experiments, per-
1030 haps most notably the 2015 Nobel prize winning particle physics experiment, Super-Kamiokande.
1031 Two detectors were placed in the Super-Kamiokande control room for 8 hours, and connected
1032 together via a 6-inch 3.5 mm audio cable in configuration (c) of Fig. 12. The data was recorded
1033 from the coincidence detector through the import_data.py, directly to a laptop. Using the same
1034 detectors and set-up, a rate measurement was also performed outside the Kamioka mine in
1035 the observatory dormitory and in the airplane at 36,000 ft when travelling between Warsaw to
1036 Tokyo. Fig. 24 shows the trigger rate of the *coincident* detector for these three measurements,
1037 as a function of calculated SiPM peak voltage.

1038 The total number of measured coincident events measured inside the Super-Kamiokande control
1039 room was found to be 101. It was found that 96% of these events were found to be located
1040 below the 50 mV peak described in Sec. 6.1, indicating that these are likely not minimum
1041 ionizing cosmic ray muons.

1042 The average rock density in the mine was measured to be 2.7 g/cm^3 , corresponding to approx-
1043 imately 2,700 m.w.e. (meter-water equivalent) of overburden[7]. Based on this, we expect the
1044 cosmic ray muon rate to be attenuated by a factor of 10^5 compared to a ground level measure-
1045 ment. With this assumption, we only expect approximately 0.04 cosmic ray muon events over
1046 the 8-hour measurement in the Super-Kamiokande control room.

1047 The master detector count rate did not significantly change when it was brought into the mine,

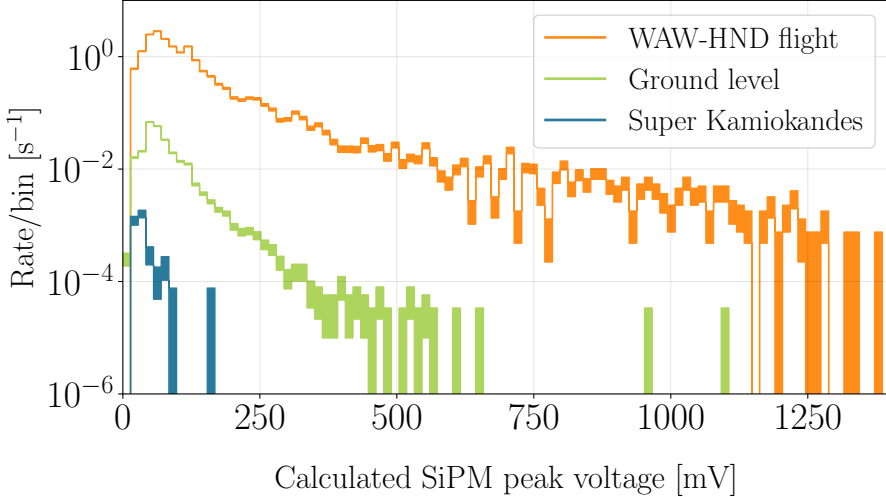


Figure 24: The measured coincidence rate at three locations. Data from Ref. [49].

1048 indicating that the radioactive background was still present in the control room. Given that
 1049 the master detector count rate was 1 Hz, Eq. 6 suggests that we should expect 1-2 accidental
 1050 coincidence events over the 8-hour period (see Sec. 6).

1051 One unaccounted background (which was briefly mentioned in Sec. 3.3) consists of events in
 1052 which a gamma-ray from a radioactive decay Compton scattered off of the scintillator of the
 1053 master detector, and was then absorbed or deposited sufficient energy in the coincident detector
 1054 scintillator. This is thought to be the dominant source of triggers in this dataset, and a Monte
 1055 Carlo simulation is currently being developed to investigate this. If these events originate from
 1056 Compton scattering, we can estimate the rate for these types of events. Given the 101 events (and
 1057 1-2 of these are assumed to be accidental coincidences and cosmic ray muons), the calculated
 1058 accidental Compton scattering coincidence rate in configuration (c) from Fig. 12 is found to be
 1059 0.0038 ± 0.0004 . A second 8-hour run was performed using the same configuration and location,
 1060 which found 92 events (with a similar SiPM peak voltage spectrum) corresponding to a count
 1061 rate of 0.0035 ± 0.0004 .

1062 This result could be further investigated by repeating the measurement, however this time with a
 1063 thin piece of lead between the scintillator. Lead, being a dense material, is likely to either absorb
 1064 the gamma-ray or absorb some of the energy from the gamma-ray through Compton scattering –
 1065 both processes would reduce the probability of measuring the event with the coincident detector.
 1066 Another potential source for these events is correlated noise. If the lead does not alter the
 1067 coincident count rate, this is a potential source for this signal, however, thus far, we have not
 1068 found any evidence of events due to noise.

1069 6.8 Cosmic ray muon angular distribution

1070 This measurement illustrates the cosmic ray muon angular dependence measured near sea level
 1071 (it was performed in Madison WI, at 266 m above sea level) and was previously described
 1072 in Ref. [49]. Here, two detectors were set to coincidence mode and placed side-by-side as in
 1073 configuration (a) of Fig. 12, spaced 52 mm apart, inside their aluminum enclosure. The distance
 1074 was chosen such that we gain sufficient statistics throughout a single day of measuring. If the
 1075 detectors are placed too far apart, the count rate drops significantly and accidental coincidences
 1076 can dominate the signal.

1077 The angle of the detectors was determined by securing the detectors to a 100 cm long rectangular
 1078 bar and then positioning the bar against a wall at a known height (see Fig. 25 (right)). It
 1079 is important when making this measurement that the angle of the detectors are accurately
 1080 measured. Fig. 25 (left) shows the measured relative rate as a function of zenith angle (with
 1081 zero radians representing vertical). Each data point represents approximately 10 hours of data
 1082 and the rate uncertainties are statistical. The horizontal uncertainties represent the calculated
 1083 opening angle of the two detectors when spaced 52 mm apart. The measurement at $\theta = \pi/2$ is
 1084 divided by 2, since at this angle it accepts cosmic-ray muons from both directions, whereas all
 1085 the other angles only accept down going muons.

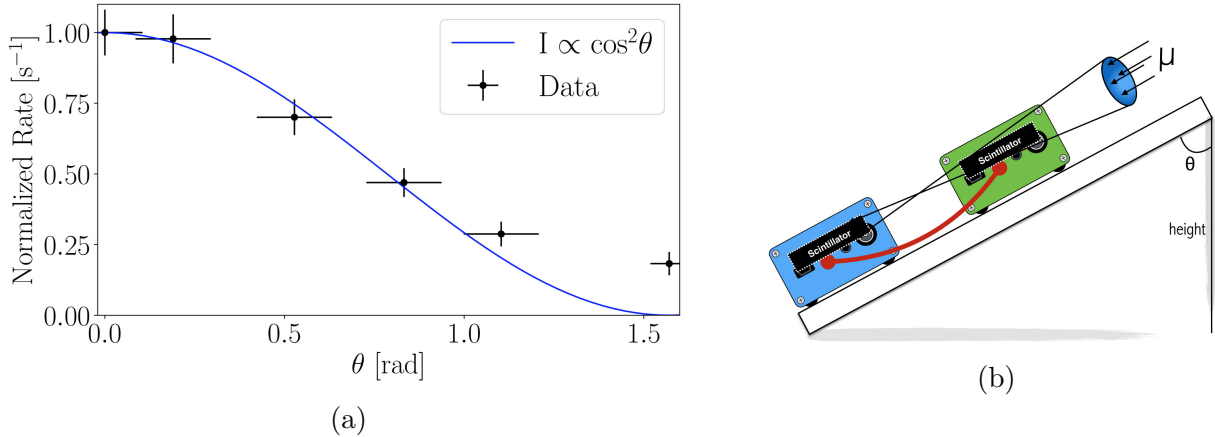


Figure 25: The measured cosmic ray muon angular distribution measured by the coincident detector when connected in coincidence mode. The prediction by the PDG is shown in solid blue. From Ref. [49].

1086 As indicated in Sec. 2.1.2, the angular cosmic ray muon dependence at sea level should follow
 1087 a cosine squared dependence. The overall measured shape of the distribution is found to agree
 1088 relatively well with the cosine squared prediction, however it is shown that the rate does not
 1089 fall completely to zero in the horizontal configuration ($\theta = \pi/2$). This is currently under
 1090 investigation, and could be related to large cosmic ray showers, showers developing in the roof
 1091 above the detector, or perhaps muons producing either high energy electrons or photons along
 1092 the track that can trigger both detectors.

1093 **6.9 Electromagnetic component of cosmic ray showers**

1094 We've discussed in Sec. 2.1 that at sea level, there is still have a flux of electrons and positrons
1095 (with energies $< 1\text{GeV}$) showering down on the Earth. We then discussed in Sec. 3.2 that this
1096 electromagnetic component is not particularly penetrating and can be significantly attenuated
1097 with a few tens of cm of concrete (the radiation length in concrete found in Table 1 is 10.7 cm).
1098 We can test this claim by measuring the coincidence rate on top of a building, then again several
1099 floors lower.

1100 We expect a minimal attenuation of the comic ray
1101 muons, however a significant attenuation of the
1102 electromagnetic component. A typical building
1103 may have 15 cm of concrete between each floor. If
1104 we measure the vertical muon rate on the top floor,
1105 then again 5 floors lower, we expect the energy of
1106 the electromagnetic component to be attenuated
1107 by 7 radiation lengths (a factor of 1000).

1108 Two detectors were place in coincidence mode one-
1109 on-top of the other in configuration (c) of Fig. 12.
1110 They were placed on the roof-top of the 10-floor
1111 WiPAC building for 24-hours inside a plastic bag
1112 to protect them against the weather. After the
1113 measurement, the same two detectors were placed
1114 on the 5th floor, and the measurement was re-
1115 peated. The results of the measurement are shown
1116 in Fig. 26.

1117 We see that the rate on top of the building is 27% higher than that of the measurement made on
1118 the 5th floor. The attenuation of this component is thought to be mostly due to the elimination
1119 of the electromagnetic component. In Sec. 2.1, we explain that approximately 33% of the total
1120 flux from cosmic ionizing radiation at sea level comes from the electromagnetic component.

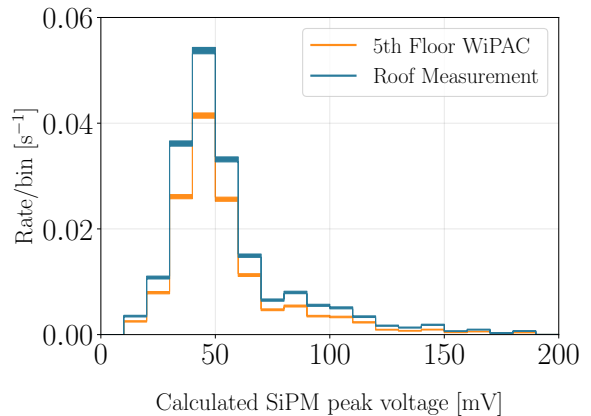


Figure 26: The calculated SiPM peak voltage on the roof of the WiPAC building compared to on the 5th floor.

1121 **6.10 Correlation between the cosmic ray muon rate and atmospheric
1122 pressure**

1123 A correlation exists between the atmospheric pressure and the cosmic ray muon rate. It can be
1124 expressed as follows:

$$\frac{\Delta I}{\bar{I}} = \beta \Delta P, \quad (6)$$

1125 where I represents cosmic ray muon intensity, ΔP is the measured atmospheric pressure com-
1126 pared to the average pressure, and β is the barometric coefficient [61]. This correlation is actually
1127 the result of several processes outlined in Sec. 2.1.2. The barometric coefficient represents the
1128 percent change in detector count rate per hPa change in atmospheric pressure.

1129 For this measurement, we decided to use an array of master-coincident detectors to improve the
1130 statistics. Five pairs of detectors were each connected in configuration (c) of Fig. 12, and left
1131 to record the cosmic ray muon rate over the course of 24.8 days (from 13:35 hrs Nov. 12th to
1132 09:00 hrs Dec. 7th 2018.). Data was recorded directly to a microSD card and powered through
1133 an 8-way USB hub powered through a wall outlet. Since the Arduino does not keep accurate
1134 time over long time-scales, we assume the time drifts linearly with time, and scale the uptime
1135 of all detectors such that they are all the same. This is not ideal, and we would recommend
1136 recording the data directly to a computer through the import_data.py in the future to get an
1137 accurate time stamp on all events. The array of detectors was placed in the 4th floor WiPAC
1138 lab in Madison, WI. Atmospheric pressure for Madison was found in Ref. [62].

1139 Fig. 27 (left) shows the correlation between the detector count rate and the atmospheric pressure.
1140 The calculated correlation is shown in the dotted white line. A least squares fit yielded a
1141 barometric coefficient of $-0.141 \pm 0.007 \text{ \%}/\text{hPa}$, in agreement with Ref. [63].

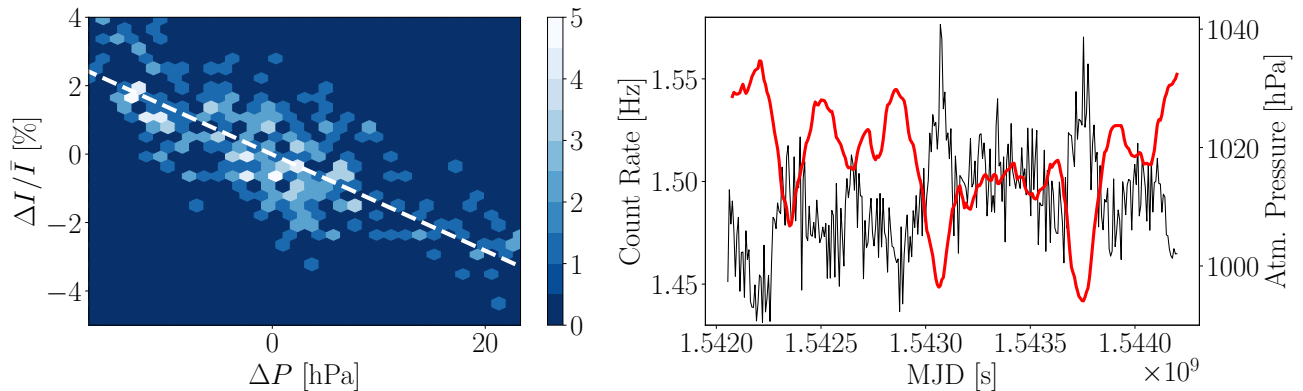


Figure 27: Left: The correlation between the atmospheric pressure and the detector count rate. Right: The detector count rate in blue and the atmospheric pressure in red as a function of modified Julian date (MJD). Both plots show the data binned with a bin size of two hours.

1142 6.11 Reducing the radioactive backgrounds

1143 It can be difficult to shield against the natural radioactivity found in the environment. Typically
 1144 at sea level, the largest component of our signal comes from radioactive backgrounds and
 1145 therefore it would be useful to think about how we can minimize this to improve the purity of
 1146 the cosmic ray muon component of the signal (beyond setting detectors into coincidence mode).

1147 Dense material placed around the detector can attenuate the incoming flux from the background radiation.
 1148 Ideally, we would choose a material that itself is radio-pure, however we can illustrate the
 1149 effect using bricks of lead. Six lead ingots (each measuring 2" x 4" x 8") were positioned in such a way
 1150 to provide 4π coverage around a single detector.
 1151 The detector recorded data directly to the microSD card throughout a full day. It was then placed
 1152 on a workbench in the same room (far away from the lead), to measure the background spectrum for
 1153 another full day. The resulting calculated SiPM
 1154 peak voltage for the two measurements is shown in Fig. 28. As expected, this is shown to significantly
 1155 reduce the event that contribute to the low SiPM peak voltage region which is dominated by
 1156 the radioactive background.
 1157

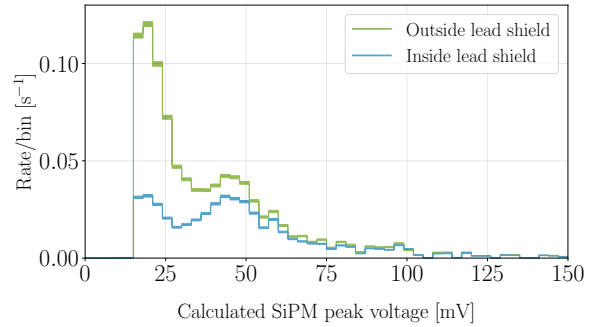


Figure 28: The effect of surrounding a single detector in a lead enclosure.

1158 another full day. The resulting calculated SiPM
 1159 peak voltage for the two measurements is shown in
 1160 Fig. 28. As expected, this is shown to significantly
 1161 reduce the event that contribute to the low SiPM peak voltage region which is dominated by
 1162 the radioactive background.

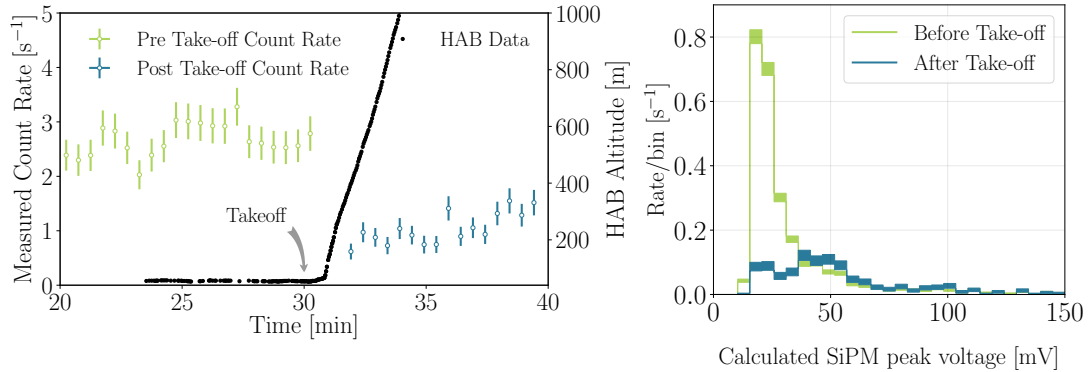


Figure 29: Left: The master detector count rate from the HAB measurement of Sec. 6.3 near take-off. Right: The calculated SiPM peak voltage for pre and post take off. Pre-take-off shown in green, and post take-off shown in blue.

1163 Another measurement that illustrates the effect of background radiation unexpectedly came
 1164 from the HAB flight described in Sec. 6.3. When the balloon pulled the detectors off of the
 1165 ground, there was a significant decrease in the master detector trigger rate as shown in Fig. 29
 1166 (left). Fig. 29 (right) shows the calculated SiPM peak voltage just prior to take-off and after
 1167 take-off. After take-off, we see the decrease in count rate came from the low-voltage region
 1168 which we've indicated primarily consists of the background radiation (see Sec. 6.1).

1169 6.12 Common sources of radioactivity

1170 Some common commercially available materials contain radioactive isotopes. Most of them
1171 originate in some form from the daughters of uranium and thorium decay. Table 2 shows a list
1172 we've compiled of items that we have found to contain a measurable amount of radioactivity
1173 using the detectors.

Table 2: Commercially available radioactive sources that are capable of triggering the detectors.
Further details will be added later.

Material	Description
Thorium welding rod	
Thorium lantern net	
Decorative Uranium beads	
Fiesta diner wear	
Uranium glassware	
Potassium salts	
Uranium ores	
Granite	
Old wrist watches	
Tritium wrist watch	
Apricots or Bananas	

1174 Beyond the list above, it can be instructional to show that the detector isn't sensitive to alpha
1175 radiation. Some smoke detectors contain Americium which is an alpha emitter, and when placed
1176 near the detector, the rate was found not to significantly change. There are also commercially
1177 available radioactive button source kits as well that can be educational. Using radioactive
1178 sources, we can also illustrate the $1/r^2$ (where r represents the distance between the scintillator
1179 and the radioactive source) fall off with distance away from the source.

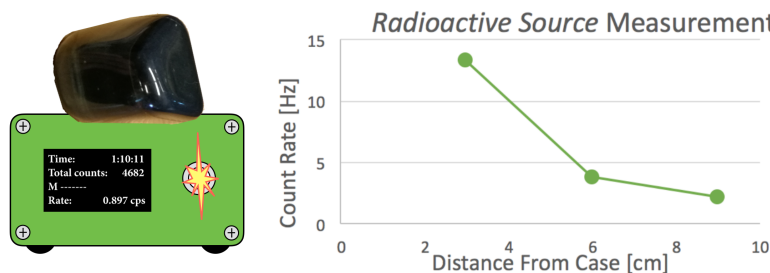


Figure 30: The measured trigger rate as a function of distance between using a rock containing uranium and a detector.

1180 **6.13 Portable trigger system for an accelerator beamline**

1181 This measurement was previously described in Ref. [49] and represents a practical use for the
1182 Desktop Muon Detectors.

1183 A single detector, powered by a 10,000 mAh USB power bank, was placed in the Fermilab M-
1184 Test facility to trigger on secondary particles (GeV-scale pions and electrons) from the Main
1185 Injector. The purpose of this was to trigger a downstream data acquisition system for another
1186 experiment. The BNC output at the back of the detector is the raw SiPM pulse which has a few
1187 nanoseconds rise time and a decay time of roughly $0.5 \mu\text{s}$. This signal is useful for experiments
1188 that want to use a scintillators but require tens of nanosecond timing. The BNC output was
1189 connected to an 80 ft BNC cable to a NIM (Nuclear Instrument Module) rack . The signal
1190 passed through a $\times 10$ amplifier and into a discriminator. If the amplified signal was above a
1191 certain value, a binary signal was sent to a AND gate, where it was compared against another
1192 scintillator paddle trigger that was located on the other side of the other experiment. If the
1193 AND condition was satisfied (ie. the particle passed through both the scintillator paddle and
1194 the Desktop Muon Detector) a binary signal was sent to the data acquisition system that began
1195 the recording of data of the downstream experiment. Fig. 31 shows the trigger rate as a function
1196 of time; the beam spills occur every minute for two seconds.

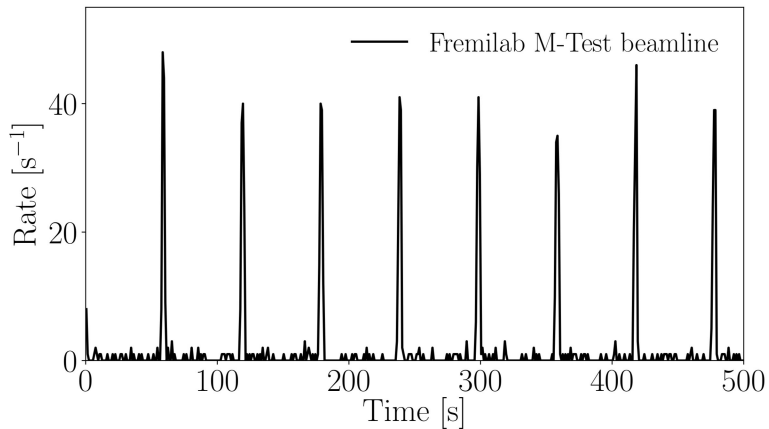


Figure 31: The trigger rate as a function of time of a single detector placed in the Fermilab M-Test beamline. Here, the detector is triggering primarily on GeV-scale pions and electrons from the Fermilab Main Injector.

1197 The detector was found to be a useful beamline trigger due to its simplicity. This ability was
1198 made possible by including a BNC output connected directly to the SiPM. For this measurement,
1199 the approximate 10 ns uncertainty in the trigger was acceptable, however if users would like to
1200 use the FAST output of the SiPM, the SiPM PCB could be modified to get down to single ns
1201 precision. We plan on investigating this sometime in the future.

1202 6.14 A true random number generator

1203 Many applications require random numbers. Often, a random number may be generated through
 1204 some algorithm, but this therefore becomes deterministic since if the user knew the algorithm
 1205 and starting conditions, they could determine the output. A random number generator would
 1206 ideally be generated from a random process, such as the arrival times of cosmic ray muons or
 1207 the decay of an isotope. The sum of two random processes will also be random, such as the
 1208 background data from the detectors. Here, I'm following the description found in Ref. [9].

1209 Any number can be expressed in terms of a sequence of ones and zeros, this is known as binary.
 1210 An N-length sequence is able to represent a number from zero to 2^N . For example, the 4-bit
 1211 binary sequence “1011”, corresponds to $1 \times (4^3) + 0 \times (3^2) + 1 \times (2^2) + 1 \times (1^2) = 8 + 0 + 2 + 1 = 11$.

1212 We can convert the time stamp of a radioactive decay trigger into a “1” or a “0” using a *toggle*
 1213 *flip-flop*. The toggle flip-flop is simply a state that changes from one to zero periodically (we will
 1214 use a frequency of 1 kHz). If a particle passes through the scintillator during an even time stamp
 1215 (as measured in milliseconds), we assign it a “1”, if it passes through an odd time stamp, we
 1216 assign it a “0”. After N triggers, we can build an N-bit random number. This is schematically
 1217 illustrated in Fig. 32.

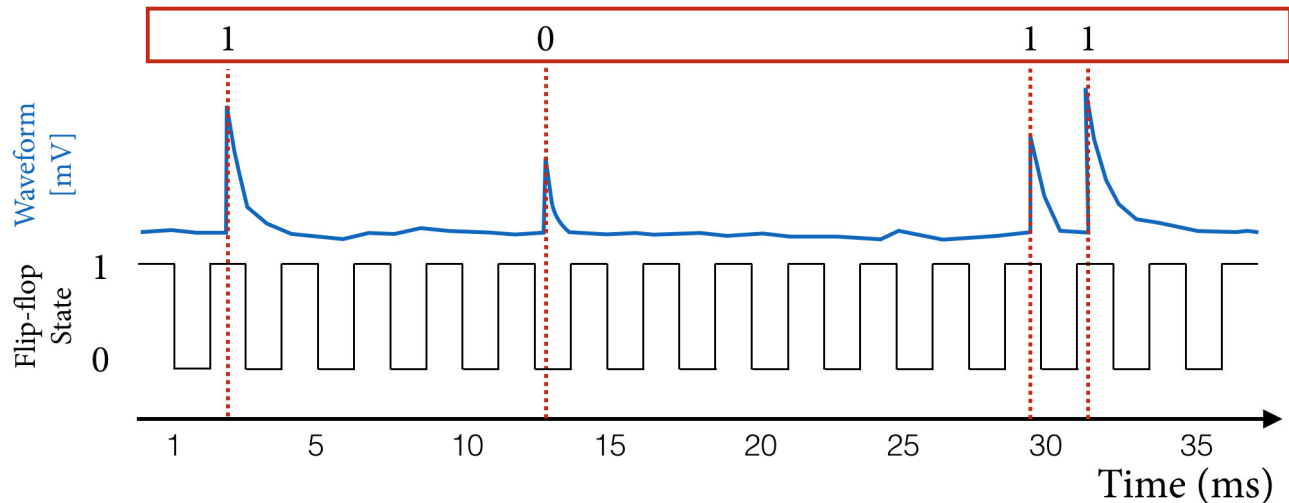


Figure 32: An illustrative diagram of the principle behind the random number generator. The x-axis indicates the time measure in milliseconds. Above this, we have the toggle flip-flop which changes state every millisecond, then an illustrative waveform shown in blue. If the event triggered the detector while in the even state of the flip flop, we assign it a one, otherwise, we assign it a zero. This is shown in the red box at the top of the diagram.

1218 For this measurement, we use data taken from a 20-day background lab measurement. A single
 1219 detector was used. After triggering on t total events, we can build t/N N-bit random numbers.
 1220 To illustrate this, if we chose to generate 8-bit random numbers (from 0 to 255), we can plot
 1221 the number of each occurrence. This is shown in Fig. 33.

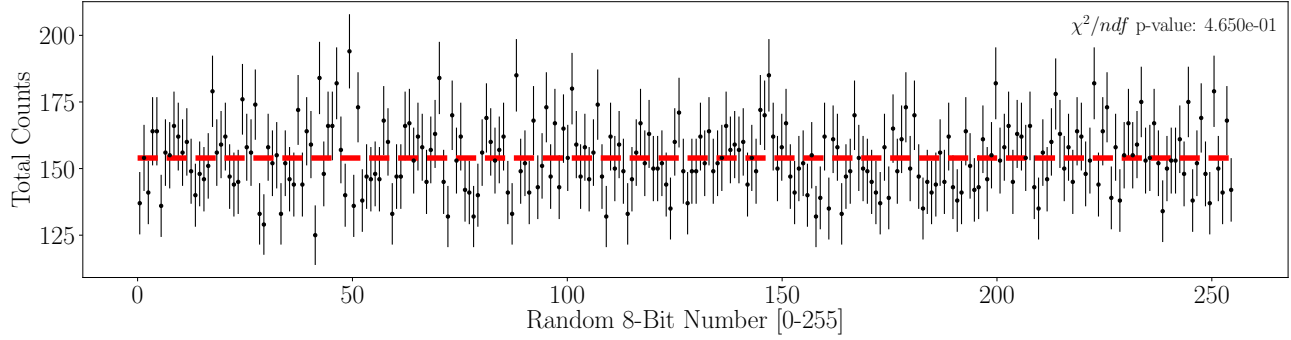


Figure 33: The number of occurrences of the generated numbers from 0-255. The reduced χ^2 assuming that the distribution should be randomly distributed about the average number of occurrences is given at the top right of the figure.

1222 Fig. 33 shows the random nature of the triggers. Each number should be equally probable to
 1223 occur. The reduced χ^2 indicates a p-value for this assumption shown in the top right of the
 1224 plot.

1225 There are several ways that the random number generator can become biased. First, let's think
 1226 about extreme scenarios. Suppose that the trigger rate is roughly 1 Hz, and the flip-flop state
 1227 only changes every 10 seconds. The first roughly ten triggers would give all ones, then the next
 1228 roughly triggers would give all zeroes. The first numbers would be biased high, while the later
 1229 numbers would be biased low. With this extreme example, we see that we need the toggle flip-
 1230 flop to be changing states at a much higher rate than the trigger rate. Secondly, suppose that
 1231 the Arduino does not produce equal numbers of even and odd time stamps due to the internal
 1232 configuration. We found this to be the case when using the microseconds() Arduino function,
 1233 that is, it only reported the time stamp to the nearest even microsecond.

1234 **6.15 The Poissonian nature of radioactive decay**

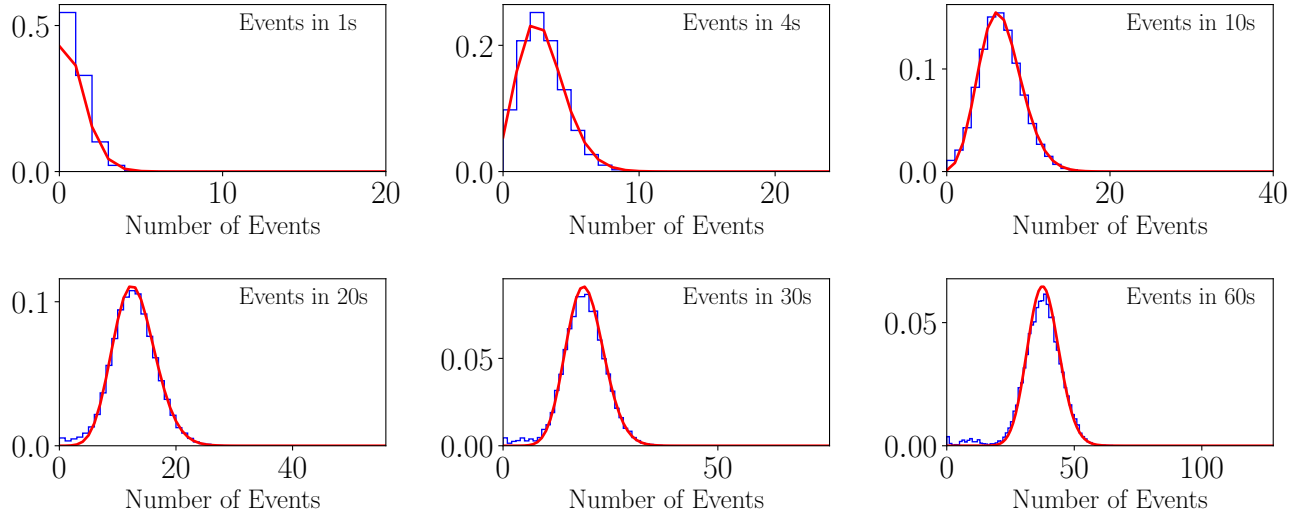


Figure 34: The distribution of count rates, where every entry is measured in a binning time which is labeled at the top right of each cell. The red line is the expected distribution if the data follows Eq. 6.

1235 A Poissonian process is one in which an event happens
 1236 that is completely independent of the occurrence of an-
 1237 other event. This is the case for many processes in na-
 1238 ture: for example, when atom decays, or the arrival
 1239 times of cosmic rays. The expected probability of ob-
 1240 serving N events in a time interval t of a Poissonian
 1241 process, with an average count rate μ is defined by the
 1242 *Poisson distribution*, Eq. 6.

1243 This example uses the same dataset from the previous
 1244 measurement, however, here we bin the data into bins
 1245 of width t and then histogram the number of measured
 1246 events in that time window. This is shown in Fig. 34.

1247 If a process is Poissonian, the time between successive
 1248 events will follow an exponential. This means that the
 1249 most likely time to observe a radioactive decay occurs
 1250 immediately. A plot of the livetime between successive
 1251 events is shown in Fig. 35 with a fitted exponential.

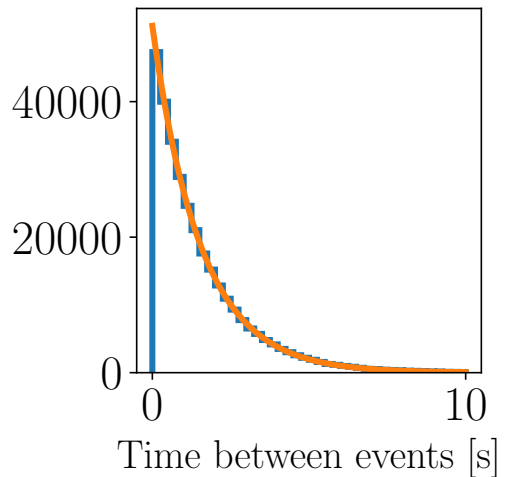


Figure 35: The time between events with an exponential fit.

1252 **6.16 Future measurements**

1253 This section compiles a list of potential future experiments that we intend to perform. After
1254 gather and analysing the data, these will be added into Sec. 6.

- 1255 1. **Muon rate underwater:** Physicists typically report the equivalent overburden in terms
1256 of how much water would provide the equivalent shielding. A measurement in actual
1257 water can be useful since it provides a homogeneous material and is abundant. We will
1258 attempt to measure the attenuation as a function of depth in a deep lake/ocean. Initially,
1259 we should observe a steep decrease due to the electromagnetic component dropping out,
1260 then a slow decrease as a function of depth.
- 1261 2. **Subway measurement:** Subways are typically buried under a significant amount of
1262 concrete and soil. A measurement at different subways could be interesting since it is
1263 easily accessible.
- 1264 3. **Cosmic ray muon rate at different floors of a large concrete building:** Large
1265 concrete buildings, like FermiLab would be great to measure the floor to floor vertical
1266 attenuation.
- 1267 4. **Special relativity measurement:** A repeat of the measurement that confirmed special
1268 relativity by measuring the muon rate on top and at the bottom of a mountain. This can
1269 be demonstrated using the altitude data here; however, climbing a mountain would make
1270 a good story.
- 1271 5. **Thin lead measurements.** Thin lead sheets, above the coincidence detectors will ac-
1272 tually cause an increase in the count rate. This is due to the muon creating a shower of
1273 secondaries, that spread out and are able to trigger the detectors simultaneously. After a
1274 few inches of lead, the shower is attenuated.
- 1275 6. **Clean room background measurement.** Background measurement in clean room at
1276 SNO+, also a coincidence measurement.
- 1277 7. **Measure the Southern Atlantic Anomaly.** This could be performed by flying from
1278 Mexico to northern Africa.
- 1279 8. **Extreme weather events:** Measure muon rate during a low pressure event – like a
1280 hurricane.
- 1281 9. **Solar flare events:** Capture data during an intense solar flare.
- 1282 10. **Solar activity:** There is an 11-year due to the solar activity that modulates the low
1283 energy cosmic rays.

1284 **7 Conclusion**

1285 The CosmicWatch Desktop Muon Detectors are capable of exploring various physical phenomena
1286 in nature. This document outlined in detail the physical processes that influence the detector,
1287 and how they can be extracted from data. We have investigated various phenomena associated
1288 with the geomagnetic field, atmospheric conditions, cosmic ray shower composition, attenuation
1289 of particles in matter, radioactivity, and statistical properties of Poissonian process. Beyond this,
1290 the supplementary material contains further information for developing skills in the machine and
1291 electrical shop, as well in programming. As the CosmicWatch program grows, we expect more
1292 people to contribute to potential measurements and improvements to the detectors. This will
1293 benefit the hundreds to thousands of students already building their own CosmicWatch Desktop
1294 Muon Detectors and learning about physics.

1295 **8 Acknowledgements**

1296 This work was supported by grant NSF-PHY-1505858 (PI: Prof. Janet Conrad), MIT seed
1297 funding, and funds from the National Science Centre, Poland (2015/17/N/ST2/04064). The
1298 authors would like to thank SensL (currently On Semiconductor) and Fermilab, for donations
1299 that made the development of this project possible, as well as P. Fisher at MIT and IceCube
1300 collaborators at WIPAC, for their support in developing this as a high school and undergraduate
1301 project. We would also like to thank Prof. Scott A. Hughes from MIT for helping in the
1302 development of this document.

1303 **9 FAQ**

1304 **What about *Cherenkov* radiation?** Cherenkov radiation occurs when a particle is passing
1305 through a material faster than the speed of light in that material. For the case of Polystyrene,
1306 this corresponds to $0.63 c$. Since the vast majority of our particles of interest are faster than
1307 $0.63c$, we expect some amount of Cherenkov radiation. However, the energy deposited in the
1308 scintillator will be nearly four orders of magnitude lower than the collisional energy from the
1309 ionizing particle.

1310 **Gamma-ray spectroscopy?:** We are often asked if the detectors are suitable for gamma-
1311 ray spectroscopy. Several attempts have been made to distinguish between gamma-emitters,
1312 however we've found that they tend to populate the low voltage region such that we do not have
1313 the resolution to identify their energy. Beyond this, the plastic scintillator is not very dense
1314 and therefore the dominate reaction from a gamma ray will be to Compton scatters, and likely
1315 penetrate the full scintillator only depositing a fraction of its energy.

1316 **References**

- 1317 [1] K. O. et al, "Cosmic rays - particle data group," *Nuclear Instruments and Methods in*
1318 *Physics Research Section A: Accelerators, Spectrometers, Detectors and Associated Equipment*, vol. 38, no. 090001, p. 6, 2014.
- 1320 [2] S. K. LBNL, "32. passage of particles through matter,"
- 1321 [3] B. Rossi, "Cosmic rays," 1964.
- 1322 [4] M. W. Friedlander, *A thin cosmic rain: Particles from outer space.* Harvard University
1323 Press, 2002.
- 1324 [5] P. K. Grieder, *Cosmic rays at Earth.* Elsevier, 2001.
- 1325 [6] T. K. Gaisser, R. Engel, and E. Resconi, *Cosmic rays and particle physics.* Cambridge
1326 University Press, 2016.
- 1327 [7] M. Fukugita and T. Yanagida, *Physics of Neutrinos: and Application to Astrophysics.*
1328 Springer Science & Business Media, 2013.
- 1329 [8] W. R. Leo, *Techniques for nuclear and particle physics experiments: a how-to approach.*
1330 Springer Science & Business Media, 2012.
- 1331 [9] C. Grupen and B. Shwartz, *Particle detectors*, vol. 26. Cambridge university press, 2008.
- 1332 [10] D. Bird, S. Corbató, H. Dai, B. Dawson, J. Elbert, T. Gaisser, K. Green, M. Huang,
1333 D. Kieda, S. Ko, *et al.*, "Evidence for correlated changes in the spectrum and composition
1334 of cosmic rays at extremely high energies," *Physical review letters*, vol. 71, no. 21, p. 3401,
1335 1993.
- 1336 [11] G. Taubes, "Pattern emerges in cosmic ray mystery," *Science*, vol. 262, no. 5140, pp. 1649–
1337 1650, 1993.
- 1338 [12] K. Greisen, "End to the cosmic-ray spectrum?," *Physical Review Letters*, vol. 16, no. 17,
1339 p. 748, 1966.
- 1340 [13] G. T. Zatsepin and V. A. Kuzmin, "Upper limit of the spectrum of cosmic rays," *Journal*
1341 *of Experimental and Theoretical Physics Letters (JETP Letters)*, vol. 4, no. 3, pp. 78–80,
1342 1966.
- 1343 [14] F. Halzen and A. D. Martin, "Quarks and leptons," 1984.
- 1344 [15] D. Griffiths, *Introduction to elementary particles.* John Wiley & Sons, 2008.
- 1345 [16] K. A. Olive *et al.*, "Review of Particle Physics," *Chin. Phys.*, vol. C38, p. 090001, 2014.
- 1346 [17] M. Tanabashi, P. Richardson, A. Bettini, A. Vogt, L. Garren, A. J. Schwartz, K. Terashi,
1347 M. Karliner, R. S. Chivukula, T. Sjöstrand, *et al.*, "Aps: Review of particle physics," *Phys.*
1348 *Rev. D*, vol. 98, p. 030001, 2018.

- 1349 [18] T. K. Gaisser and M. Honda, "Flux of atmospheric neutrinos," *Annual Review of Nuclear*
 1350 *and Particle Science*, vol. 52, no. 1, pp. 153–199, 2002.
- 1351 [19] E. Regener and G. Pfotzer, "Vertical intensity of cosmic rays by threefold coincidences in
 1352 the stratosphere," *Nature*, vol. 136, no. 3444, p. 718, 1935.
- 1353 [20] O. Allkofer, R. Andresen, and W. Dau, "The muon spectra near the geomagnetic equator,"
 1354 *Canadian Journal of Physics*, vol. 46, no. 10, pp. S301–S305, 1968.
- 1355 [21] O. Allkofer, R. Andresen, K. Clausen, and W. Dau, "Sea-level muon spectrum at two
 1356 different latitudes," *Journal of Geophysical Research*, vol. 77, no. 22, pp. 4251–4253, 1972.
- 1357 [22] C. Augusto, C. Navia, and K. Tsui, "Muon enhancements at sea level in association with
 1358 swift-bat and milagro triggers," *Physical Review D*, vol. 77, no. 12, p. 123008, 2008.
- 1359 [23] https://www.nasa.gov/mission_pages/station/research/experiments/1043.html, "International
 1360 space station internal radiation monitoring (iss internal radiation monitoring) -
 1361 04.05.17," Dec 2018.
- 1362 [24] T. Dachev, W. Atwell, E. Semones, B. Tomov, and B. Reddell, "Observations of the saa
 1363 radiation distribution by liulin-e094 instrument on iss," *Advances in Space Research*, vol. 37,
 1364 no. 9, pp. 1672–1677, 2006.
- 1365 [25] L. Pinsky, W. Osborne, J. Bailey, R. Benson, and L. Thompson, "Light flashes observed by
 1366 astronauts on apollo 11 through apollo 17," *Science*, vol. 183, no. 4128, pp. 957–959, 1974.
- 1367 [26] A. Rinaldi, "Phosphenes in space: a study on the interaction between carbon ions and rod
 1368 photoreceptor," 2009.
- 1369 [27] C. Fuglesang, L. Narici, P. Picozza, and W. G. Sannita, "Phosphenes in low earth orbit:
 1370 survey responses from 59 astronauts," *Aviation, space, and environmental medicine*, vol. 77,
 1371 no. 4, pp. 449–452, 2006.
- 1372 [28] C. Augusto, C. Navia, H. Shigueoka, K. Tsui, and A. Fauth, "Muon excess at sea level
 1373 from solar flares in association with the fermi gbm spacecraft detector," *Physical Review*
 1374 *D*, vol. 84, no. 4, p. 042002, 2011.
- 1375 [29] M. Savić, D. Maletić, D. Joković, N. Veselinović, R. Banjanac, V. Uđovičić, and A. Dragić,
 1376 "Pressure and temperature effect corrections of atmospheric muon data in the belgrade
 1377 cosmic-ray station," in *Journal of Physics: Conference Series*, vol. 632, p. 012059, IOP
 1378 Publishing, 2015.
- 1379 [30] P. H. Barrett, L. M. Bollinger, G. Cocconi, Y. Eisenberg, and K. Greisen, "Interpretation
 1380 of cosmic-ray measurements far underground," *Reviews of Modern Physics*, vol. 24, no. 3,
 1381 p. 133, 1952.
- 1382 [31] F. An, A. Balantekin, H. Band, M. Bishai, S. Blyth, D. Cao, G. Cao, J. Cao, Y. Chan,
 1383 J. Chang, *et al.*, "Seasonal variation of the underground cosmic muon flux observed at daya
 1384 bay," *Journal of Cosmology and Astroparticle Physics*, vol. 2018, no. 01, p. 001, 2018.

- 1385 [32] A. Bouchta, "Seasonal variation of the muon flux seen by amanda," in *International Cosmic*
1386 *Ray Conference*, vol. 2, p. 108, 1999.
- 1387 [33] M. Ambrosio, R. Antolini, G. Auriemma, R. Baker, A. Baldini, G. Barbarino, B. Barish,
1388 G. Battistoni, R. Bellotti, C. Bemporad, *et al.*, "Seasonal variations in the underground
1389 muon intensity as seen by macro," *Astroparticle Physics*, vol. 7, no. 1-2, pp. 109–124, 1997.
- 1390 [34] W. Benenson, J. W. Harris, H. Stöcker, and H. Lutz, *Handbook of physics*. Springer Science
1391 & Business Media, 2006.
- 1392 [35] D. Green, *The physics of particle detectors*, vol. 12. Cambridge University Press, 2000.
- 1393 [36] W. Li, M. D. Rodriguez, P. Kluth, M. Lang, N. Medvedev, M. Sorokin, J. Zhang, B. Afra,
1394 M. Bender, D. Severin, *et al.*, "Nu clear instrum ents and methods in phy sics research b,"
1395 *Nuclear Instruments and Methods in Physics Research B*, vol. 302, pp. 40–47, 2013.
- 1396 [37] B. R. Martin, *Nuclear and particle physics: an introduction*. John Wiley & Sons, 2006.
- 1397 [38] T. Tabata, R. Ito, and S. Okabe, "An empirical equation for the backscattering coefficient
1398 of electrons," *Nuclear instruments and methods*, vol. 94, no. 3, pp. 509–513, 1971.
- 1399 [39] M. J. Berger and S. M. Seltzer, "Stopping powers and ranges of electrons and positions,"
1400 tech. rep., NATIONAL STANDARD REFERENCE DATA SYSTEM, 1982.
- 1401 [40] https://www.onsemi.com/pub/Collateral/AND9770_D.PDF, "On semiconductor: Introduction
1402 to the silicon photomultiplier," Dec 2018.
- 1403 [41] <https://www.sensl.com/downloads/ds/TN> "Sensl: An introduction to the silicon photomul-
1404 tiplier," Dec 2018.
- 1405 [42] A. Pla-Dalmau, A. D. Bross, V. V. Rykalin, and B. M. Wood, "Extruded plastic scintil-
1406 lator for minerva," in *Nuclear Science Symposium Conference Record, 2005 IEEE*, vol. 3,
1407 pp. 1298–1300, IEEE, 2005.
- 1408 [43] Eljen. <https://eljentechnology.com/products/plastic-scintillators>, accessed: Oct 2018 2018.
- 1409 [44] H. Yang, D. Cao, Z. Qian, X. Zhu, C. Loh, A. Huang, R. Zhang, Y. Yang, Y. Liu, B. Xu,
1410 *et al.*, "Light attenuation length of high quality linear alkyl benzene as liquid scintillator
1411 solvent for the juno experiment," *Journal of Instrumentation*, vol. 12, no. 11, p. T11004,
1412 2017.
- 1413 [45] D. Beznosko, A. Bross, A. Dyshkant, and P.-D. Rykalin, "Fnal-nicadd extruded scintilla-
1414 tor," in *Nuclear Science Symposium Conference Record, 2004 IEEE*, vol. 2, pp. 790–793,
1415 IEEE, 2004.
- 1416 [46] D. Horrocks, *Applications of liquid scintillation counting*. Elsevier, 2012.
- 1417 [47] I. Ambats, Y. Antipov, A. Sadovski, K. Lang, W. Allison, D. Wall, A. Napier, Y. Lai,
1418 R. Heinz, D. Wright, *et al.*, "The minos detectors technical design report," tech. rep., 1998.

- 1419 [48] L. Aliaga, L. Bagby, B. Baldin, A. Baumbaugh, A. Bodek, R. Bradford, W. Brooks,
1420 D. Boehnlein, S. Boyd, H. Budd, *et al.*, “Design, calibration, and performance of the
1421 minerva detector,” *Nuclear Instruments and Methods in Physics Research Section A: Ac-
1422 celerators, Spectrometers, Detectors and Associated Equipment*, vol. 743, pp. 130–159, 2014.
- 1423 [49] S. N. Axani, K. Frankiewicz, and J. M. Conrad, “The cosmicwatch desktop muon detector:
1424 a self-contained, pocket sized particle detector,” *Journal of Instrumentation*, vol. 13, no. 03,
1425 p. P03019, 2018.
- 1426 [50] DECO. <https://wipac.wisc.edu/deco/home>, accessed: Nov. 2018.
- 1427 [51] CREDO. <https://credo.science/>, accessed: Nov. 2018.
- 1428 [52] M. Bardeen, M. Wayne, and M. J. Young, “Quarknet: A unique and transformative physics
1429 education program,” *Education Sciences*, vol. 8, no. 1, p. 17, 2018.
- 1430 [53] http://www.teachspin.com/muon_physics.html, “Teachspin: Muon physics,” Dec 2018.
- 1431 [54] <https://www.arduino.cc/en/Main/Software>, “Arduino,” July 2017.
- 1432 [55] S. N. Axani, “Cosmicwatch repository.” [https://github.com/spenceraxani/CosmicWatch-
Desktop-Muon-Detector-v2](https://github.com/spenceraxani/CosmicWatch-
1433 Desktop-Muon-Detector-v2), accessed: February 2017.
- 1434 [56] Youtube. <https://www.youtube.com/watch?v=e4IXzNiNwgU>, accessed: Jan 2018.
- 1435 [57] <https://github.com/adrianmihalko/ch340g-ch34g-ch34x-mac-os-x> driver, “Ch340g driver,”
1436 July 2017.
- 1437 [58] Flight Aware. <https://flightaware.com/>, accessed: Dec. 2017.
- 1438 [59] <http://nearspace.pl/>, “Near space conference 2018,” Dec 2018.
- 1439 [60] K. Albrecht *et al.* (The IceCube Collaboration), “IceCube - the next generation neutrino
1440 telescope at the South Pole,” *Nuclear Physics B-Proceedings Supplements*, vol. 118, pp. 388–
1441 395, 2003.
- 1442 [61] R. De Mendonca, J.-P. Raulin, E. Echer, V. Makhmutov, and G. Fernandez, “Analysis
1443 of atmospheric pressure and temperature effects on cosmic ray measurements,” *Journal of
1444 Geophysical Research: Space Physics*, vol. 118, no. 4, pp. 1403–1409, 2013.
- 1445 [62] LocalConditions.com. [https://www.localconditions.com/weather-madison-
1446 wisconsin/53701/past.php](https://www.localconditions.com/weather-madison-wisconsin/53701/past.php), accessed: Dec. 2018.
- 1447 [63] K. Jourde, D. Gibert, J. Marteau, J. de Bremond d’Ars, S. Gardien, C. Girerd, and J.-C.
1448 Ianigro, “Monitoring temporal opacity fluctuations of large structures with muon radiog-
1449 raphy: a calibration experiment using a water tower,” *Scientific reports*, vol. 6, p. 23054,
1450 2016.